KeAi

CHINESE ROOTS
GLOBAL IMPACT

Contents lists available at ScienceDirect

Petroleum Science

journal homepage: www.keaipublishing.com/en/journals/petroleum-science



Original Paper

Paleo-fluid evolution in the Lower-Middle Ordovician carbonate reservoirs of the Shunbei area, Tarim Basin



Bai-Wen Huang ^a, Ning Ye ^{a, *}, Zi-Ye Lu ^a, Bei Zhu ^a, Yi-Ming Yang ^b, Pan Lin ^c, Pei-Jie Li ^d, Xin-Yan Zhang ^b, Ying-Tao Li ^e, Shao-Nan Zhang ^a

- ^a School of Geoscience and Technology, Southwest Petroleum University, Chengdu, 610500, Sichuan, China
- ^b PetroChina Southwest Oil and Gas Field Company, Chengdu, 610051, Sichuan, China
- ^c Research Institute of Exploration and Development, Southwest Branch Company, Sinopec, Chengdu, 610041, Sichuan, China
- ^d Jidong Oilfield Company, PetroChina, Tangshan, 063000, Hebei, China
- ^e SINOPEC Exploration and Production Research Institute, Beijing, 10083, China

ARTICLE INFO

Article history: Received 27 March 2024 Received in revised form 3 November 2024 Accepted 13 March 2025 Available online 17 March 2025

Edited by Jie Hao

Keywords: Calcite cements Geochemistry Paleo-fluid flows Shunbei area Tarim basin

ABSTRACT

Deep carbonate reservoirs affected by prominent strike-slip faults represent crucial targets in oil and gas exploration owing to their immense resource potential. However, the complex geological environments and poorly understood histories of the associated paleo-fluid activity have hindered the development of robust theories regarding pore formation and preservation mechanisms, resulting in suboptimal exploration strategies. Leveraging the extensive well deployment by the China Sinopec Group in the Shunbei area of the Tarim Basin, this study addresses these challenges by establishing a comprehensive framework for the evolution of diagenetic fluids within the Middle-Lower Ordovician carbonate formations. Using core samples, thin-section analysis, and cathodoluminescence observations, this study employs high-resolution geochemical methodologies, including isotopic analyses, rare earth element profiling, fluid inclusion studies, and uranium-lead dating, as primary tools for identifying and interpreting paleo-fluid characteristics across various rock types and calcite cement varieties within this stratigraphic interval. The findings reveal several key insights: (i) both RFC and C1 cements are derived from seawater, with C1 forming under burial conditions; (ii) C2, C3, and VC cements result from distinct tectonic events, specifically during the first and third episodes of the Middle Caledonian movement, with meteoric water infiltrating fault systems independently of orogenic belts or paleo-karst systems; and (iii) previous conclusions are challenged, as the influence of hydrothermal activity in this area is found to be minimal. Furthermore, the model presented here serves as a valuable reference for understanding fluid activity events at distal locations within orogenic belts under compressive stress, while accurately capturing fluid variations over different temporal scales within fault zones plays a decisive role. © 2025 The Authors. Publishing services by Elsevier B.V. on behalf of KeAi Communications Co. Ltd. This is an open access article under the CC BY-NC-ND license (http://creativecommons.org/licenses/by-nc-nd/ 4.0/).

1. Introduction

The correlation between faults and associated paleo-fluid flow has become a key focus area in oil and gas exploration over the past decade, as fluids often infiltrate the host rock through intricate fault systems, altering the subsurface environment (Balsamo et al., 2012; Hodson et al., 2016; Navarro-Ciurana et al., 2016). Theoretically, the complex interplay between hydrology and hydrochemistry leads to initial crystal dissolution, ion migration/diffusion, and subsequent

* Corresponding author. E-mail address: yn870104@foxmail.com (N. Ye). crystal precipitation within the water-rock system, which transforms the reservoir space morphology and distribution. This process continues until a relative dynamic equilibrium is reached at the macroscopic level in terms of temperature, ion concentration, and salinity (Machel, 2004; Ehrenberg and Bjørlykke, 2016). To accurately predict the locations of extensive pore development, petroleum geologists have focused on analyzing strike-slip fault activity inversion and the associated fluid evolution processes (Qing and Mountjoy, 1992; Yapparova et al., 2017; Stacey et al., 2021). This is primarily due to the pressure release from strike-slip fault activity, which significantly enhances the capacity for deep-seated fluid transport. The resulting pumping and thermal

convection effects disrupt the thermal equilibrium of the original formation fluids and link various aquifers within sedimentary basins, enabling fluid mixing and circulation that can lead to the formation of large-scale reservoirs (Ehrenberg and Bjørlykke, 2016). Consequently, strike-slip zones offer an ideal setting to study the coupled 'fault-fluid' phenomenon. Fluid properties differ across structural settings and active eras, significantly impacting fluid saturation and water-rock reactions (Davies and Smith, 2006; Yapparova et al., 2017; Stacey et al., 2021). Pinpointing the origins and timelines of individual fluid phases in deeply buried reservoirs is challenging due to the complexity of fluid mixtures and task of clarifying fluid migration pathways. This underscores a critical scientific issue in understanding pore formation and preservation mechanisms within fault-controlled reservoirs.

In the past decade, significant oil and gas reserves have been discovered in ultra-deep carbonate formations (over 7000 m deep) near small-scale strike-slip faults in the Shuntuoguole Low Uplift (SLU) (Cao et al., 2020; Jia et al., 2021). This highlights the importance of NE-trending strike-slip faults and associated fluids in developing high-quality reservoirs (Deng et al., 2018; Han et al., 2021; Lv et al., 2021). Undoubtedly, research on cement remains a focal point due to its relevance in modifying fluid responses within fractures. However, several challenges persist in theories and testing methods: (i) fluid characteristics differ significantly across faulted zones. In the northern Shunbei area (SHB), cement is predominantly calcite, while in the southern Shunnan area (SN), it consists mainly of coarse quartz. These differences in mineral composition reflect variations in fluid temperature, pressure. salinity, and other factors, leading to hypotheses involving meteoric water, hydrothermal water, and syngenetic seawater/brine (Dong et al., 2013; Chen et al., 2016; Li et al., 2023); yet, a persuasive unified understanding is still lacking. (ii) Traditional whole-rock geochemistry is widely used, but even with advances in microarea sampling, several minerals exhibit complex growth-zoning structures, making it challenging to perform high-spatialresolution, multi-stage fluid inversions. Consequently, detected signals may be mixed. (iii) Lacking minerals suitable for radiometric dating, researchers often rely on other geochemical methods to obtain chronological data indirectly. (iv) Fluid inclusion petrographic data are often unpublished or minimally described, leading to an unclear correlation between measured aqueous and hydrocarbon inclusions and rendering conclusions nearly 'meaningless' (Goldstein, 2001). As a crucial component of the SLU, the SHB provides an ideal natural setting to examine the fluid evolution process via inversion. This is due to the cross-cutting calcite veins visible in most core samples extracted from drilling, capturing valuable data on fluid behavior during different tectonic events. Recent research has introduced new insights into fluid characteristics and origins (Li et al., 2023; Wang et al., 2023) and their influence on limestone alteration (Jia et al., 2021). However, much of this theory is based on SN samples. Therefore, it may not be appropriate to generalize findings across both regions, which have distinct histories of sedimentation, exposure, fluid activity, thermal events, and hydrocarbon storage. Additionally, spatial resolution issues have often been overlooked in surveys.

This study aimed to address the limitations of prior research by reconstructing the fluid activity history of the SHB. Fortunately, dependable results from prior studies enable us to provide: (i) a qualitative analysis of the characteristics, sources, and active eras of each fluid phase within major fracture zones, using trace elements (including rare earth elements), strontium isotopes, and uraniumlead dating via in-situ techniques; and (ii) a standardized model to describe and interpret the mechanism of fluid flow within a structurally controlled system. Ultimately, this study holds significant theoretical and practical implications for advancing the 'fault-

fluid coupling' concept and guiding the accurate prediction of favorable fault-controlled reservoirs.

2. Geological setting

Situated in the central Tarim Basin of China (Fig. 1(a)), the SLU is a stable palaeotectonic unit flanked by the Shaya Uplift to the north and Katak Uplift to the south, and embraced by the Manjia Depression on its eastern side and Awati Depression on its western side (Jia et al., 2021) (Fig. 1(b)). The SHB is located in the northern part of the SLU (Fig. 1(c)) and has undergone a complex evolutionary history with multi-stage tectonic evolution, particularly influenced by awe-inspiring events, such as the first and third episodes of the Middle Caledonian, followed by the Late Caledonian-Early Hercynian and the Middle-Late Hercynian movements that are most vividly and unmistakably demonstrated through these exceptional unconformities (Wang, 2022).

According to records, the SHB underwent a transition from slope-shelf to carbonate platform facies from the Cambrian to the Early Ordovician owing to regional tensile stress. This transition also resulted in the formation of weak fracture systems and normal faults (Li et al., 2013). By the end of the Middle Ordovician, influenced by the subduction of the ancient Kunlun Ocean plate in the NE direction (the first Episode of the Middle Caledonian movement), regional-scale joints and some strike-slip faults began to form, exhibiting positive flower structures in certain profiles. These structures predominantly intersected or penetrated through the Cambrian Formation and connected with the top of the Middle-Lower Ordovician (Oiu et al., 2019), Subsequently, a global transgression resulted in the significant deposition of mudstone sequences on this platform (Wang et al., 2023). The Aljin Mountain collision orogeny (the third episode of the Middle Caledonian movement) further heightened uplift and resulted in the development of a regional angular unconformity during the Late Ordovician timespan (Deng et al., 2021). In addition, this period marked the peak occurrence of regional-scale NE- and NW-trending strikeslip faults formed under compressive stress.

During the Silurian-Devonian period, the South Tianshan Ocean gradually closed due to subduction (the Late Caledonian-Early Hercynian movement), leading to the disappearance of the Ordovician to Silurian strata within a timeframe of 45–50 Ma. In addition, the initially formed strike-slip faults intensified and extended into the Middle-Lower Devonian (Song et al., 2022). Subsequently, the Middle-Late Hercynian movements caused denudation and triggered extensive volcanic and faulting activities that persisted until the end of the Permian period (Li et al., 2013). Since then, the SHB has maintained a sedimentary pattern of intercontinental depressions without significant tectonic change until the present day. This is thought to be because most stress is absorbed by substantial uplifts and faults along the basin margin (Wang, 2022).

In ascending order, the Ordovician succession comprises the Penglaiba (O_1p) , Yingshan $(O_{1-2}y)$, Yijianfang (O_2yj) , Qiaerbake (O_3q) , Lianglitage (O_3l) , and Sangtamu (O_3s) formations, showing a remarkable sedimentary transition from marine carbonates to terrestrial clastics, with a transitional point occurring after O_2yj . As previously elucidated, to pursue scientific theoretical development and meet the needs of practical exploration, our study primarily focused on the $O_{1-2}y$ and O_2yj intervals because of their abundant carbonate samples as well as the intriguing diagenetic and structural phenomena illustrated in Fig. 1(d).

3. Material and methods

Approximately 250 hand specimens were collected from $O_{1-2}y$ and O_2yj in the SHB for petrographic analysis. Standard polished

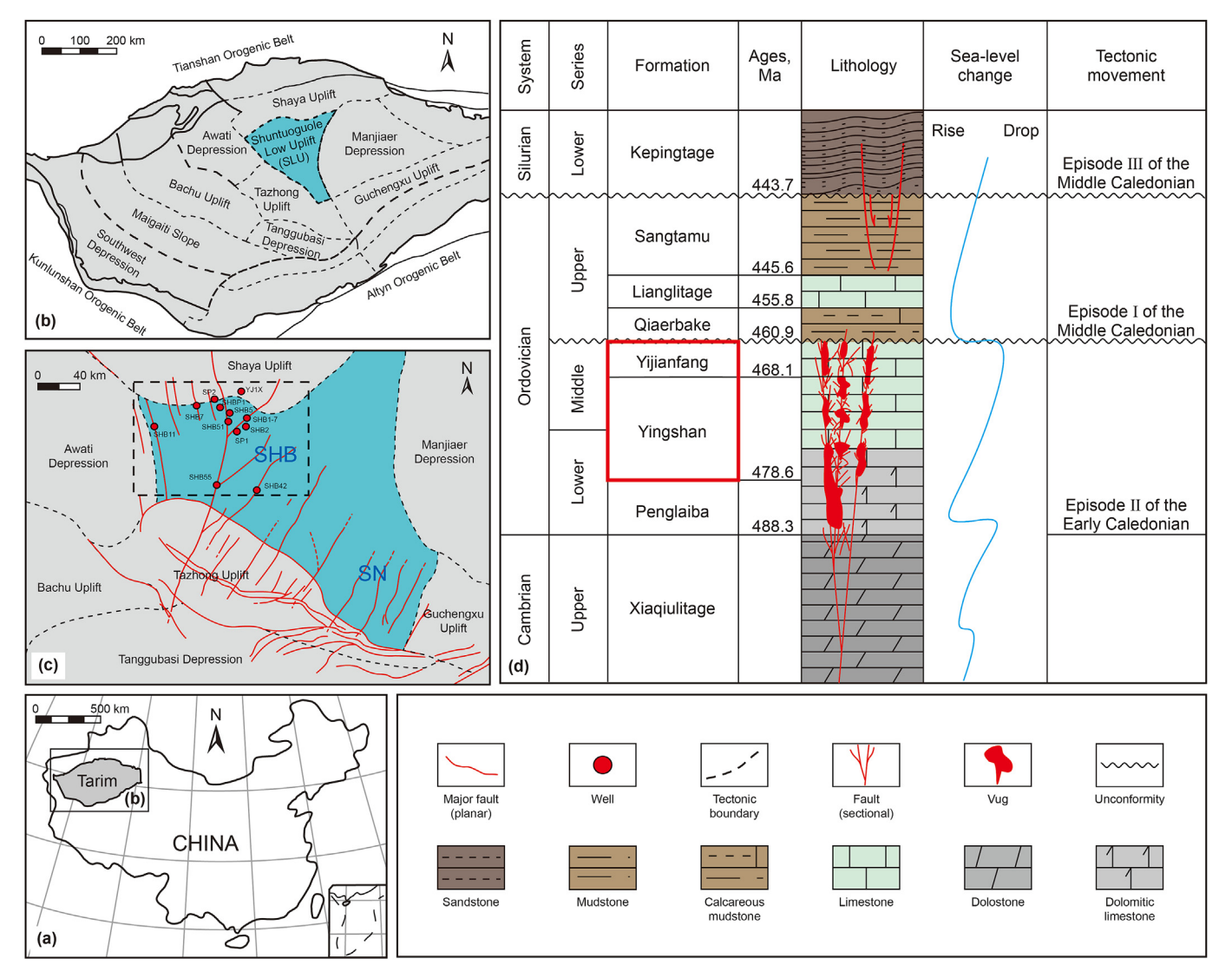


Fig. 1. (a) Cartographic depiction of China with latitude and longitude; (b) Tectonic framework of the Tarim Basin within its reginal context and spatial distribution of SLU (represented by the blue area); (c) Location of SHB (indicated by the black dotted border); (d) Stratigraphic context of SHB, with a specific emphasis on the O₁₋₂y and O₂yj (red solid border).

thin sections, 30 μm thick, were observed using the Leica DM2700 transmission and reflection microscope under normal transmission light. To differentiate between calcite and dolomite, all thin sections were stained with alizarin Red-S. The cathodoluminescence (CL) analysis was conducted at the State Key Laboratory of Oil and Gas Reservoir Geology and Exploitation of Southwest Petroleum University using a CL 8200 MK5 cathodoluminescence system with a Leica polarized light microscope at beam voltages of 5–8 kV and beam currents of 0.3–0.5 mA.

The carbon (δ^{13} C) and oxygen (δ^{18} O) isotope analyses were analyzed out on Finnigan Kiel-III apparatus connected to a Finnigan MAT 253 mass spectrometer at the Chengdu University of Technology. Approximately 50 mg of the powdered sample was reacted with 100% H₃PO₄ at 50 °C for 3 h, and then the released carbon dioxide was transferred to a MAT 253 mass spectrometer for analysis. The isotope data were recorded in standard notation relative to the Vienna Peedee Belemnite (VPDB) standard and calibrated against the NBS-18 and NBS-19 standards. The analytical precision is better than $\pm 0.1\%$ for the carbon and oxygen isotope values.

Strontium isotope (87Sr/86Sr) analysis of the whole rock was

performed using a MAT 262 solid isotope mass spectrometer at Chengdu University of Technology. The samples were powdered (approximately 100 mg) and dissolved in 2.5 N HCl. Rubidium and strontium were separated using an AG50W × 8 (H+) cationexchange resin column. The values were normalized to the NBS987 standard and the average standard error was $(2\sigma) \pm 12 \times 10^{-6}$. In addition, in situ strontium isotope analysis was performed using laser denudation multi-receiving cup inductively coupled plasma mass spectrometry (LA-MC-ICP-MS) at Wuhan Upper Spectrum Analysis Technology Co., LTD. The laser denudation system used was Geolas HD (Coherent, Germany), and the MC-ICP-MS used was Neptune Plus (Thermo Fisher Scientific, Germany). Laser denudation systems use helium as a carrier gas. The laser beam spot is 160 μm , the laser denudation rate is 8–15 Hz, and the laser energy density is fixed at approximately 10.0 I/cm². The Sr isotope instrument mass fractionation was corrected using the index rule, and the correction factor was estimated to be ${}^{88}\text{Sr}/{}^{86}\text{Sr} = 8.375209$ (Tong et al., 2016).

In situ trace elemental measurements were conducted using a combined ESI 193UC laser ablation system (ArF 193 nm gas excimer

laser) and an Agilent 7800 ICP-MS at the Laboratory of Carbonate Sedimentary and Diagenetic Geochemistry, Southwest Petroleum University. The laser-spot size and frequency of the laser were set to 80 μm and 10 Hz, respectively, in this study. Standards NIST612 and MACS-3 were used to correct for drift and check measurement uncertainties (Ca was used as an internal standard: relative REY concentration errors <10%). Data processing and calibration were performed using the Iolite software. Raw REY concentrations were normalized to Post-Archean Australian Shale (PAAS). The bellshaped index (BSI), commonly utilized to evaluate the enrichment of middle rare earth elements (MREE), was calculated following the methodology established by Tostevin et al. (2016). This index can be analyzed in conjunction with Ce and Eu anomalies to assess fluid properties (Webb and Kamber, 2000; Bau et al., 2010), with the subscript 'N' indicating normalization to PAAS. The principles are shown in Eqs. (1)–(3):

$$\begin{split} BSI &= 2 \times (Sm_N + Gd_N + Dy_N) / \left((La_N + Pr_N + Nd_N) / 3 + (Ho_N + Er_N + Tm_N + Yb_N + Lu_N) / 5 \right) \end{split} \tag{1}$$

$$(Ce/Ce*)_N = 2Ce_N/(La_N + Pr_N)$$
(2)

$$(Eu/Eu*)_N = Eu_N/(0.67Sm_N + 0.33Tb_N)$$
 (3)

Uranium-Lead dating was performed by laser ablation using a Resolution laser denudation system and a Thermo Fisher iCAP RQ inductively coupled plasma mass spectrometer at Guizhou Tongwei Analytical Technology Co., Ltd. The standard sample used for calibration was AHX-1D (age: (238.2 ± 2.4) Ma) from the Shaoerbulak Formation in Aksu area, Tarim Basin. The analytical process and standard sample analysis are described in detail by Shen et al. (2019).

4. Results

4.1. Petrography

4.1.1. Matrix rocks

Based on petrological observations and classification standards established by predecessors (Sibley and Gregg, 1987), a comprehensive categorization of matrix carbonate rocks can be discerned. These categories include grainstone (GS), wackstone (WS)/packstone (PS), micritic limestone (ML), dolomitic limestone (DL), siliceous limestone (SL), and dolostone (DS).

The GS hand specimen displays a grey hue with abundant, discernible dark particles. Under microscopic examination, the cement is typically sparry calcite and particles primarily comprise morphological bioclasts and intraclasts (Fig. 2(a)). WS and PS are more commonly observed and consist of rounded peloids and microspars (Fig. 2(b)). Additionally, ML is extensively developed, showing significant thickness and continuous distribution, with densely scattered micrite and sparse biological debris (Fig. 2(c)).

The following three lithologies, though minor (together comprising <5% of all matrix rock samples), have been meticulously observed and described in detail at the microscopic level. DL and SL represent two transitional phases of limestone. In DL, dolomites with planar-s (planar crystal face and subhedral texture) to planar-e (planar crystal face and euhedral texture) features are dispersed within a microcrystalline calcite matrix (Fig. 2(f)) or along stylolites. Conversely, SL mainly comprises cryptocrystalline chalcedony and microcrystalline quartz, which often exhibit concave-convex contact with the micrite (Fig. 2(d)) and appear as bioclasts or display non-selective patchy to complete replacement of ML. In DS, turbid crystals range from 100 to 500 μ m, transitioning from planar-s to planar-e morphology and showing a consistent extinction pattern

under cross-polarized light. Notably, intercrystalline dissolved pores are present, filled with calcite and minor quartz cements (Fig. 2(e)).

4.1.2. Calcite cements

In the fractures and pores of matrix rocks, distinct cathode luminescence and an intercutting pattern among calcites are observed. Five categories of calcite cements are identified: (i) Rediaxial fibrous calcite (RFC), which appears as isopachous cortices of one or more fibrous sublayers of length-fast calcites (Fig. 3(d) and 4(a)). RFC shows straight extinction under crossedpolarized light and exhibits faint luminescence under cathode rays (Fig. 4(b)); (ii) C1, filling fractures 50–100 μm wide, which consistently displays subdued luminescence under cathode rays (Fig. 3(a) and (b), 4(c) and (d)); (iii) C2, with crystal sizes of 100-250 µm, which internally emits dull red luminescence and displays intense red at the crystal edges (Fig. 4(c) and (d)); (iv) C3, predominantly found in high-angle fractures, is the most common type intersecting both C1 and C2 and is further intersected by largeamplitude stylolites (Fig. 3(a) and 5(a)), showing dull red luminescence (Fig. 4(d)); and (v) VC, which appears within dissolved pores of DS (100-500 µm) and intersects stylolites (Fig. 5(b)). VC also displays very faint luminescence (Fig. 5(c)), while concomitant dolomite appears relatively bright (Fig. 5(d)).

4.2. Geochemistry

4.2.1. Isotope

The isotopic compositions of carbon (δ^{13} C), oxygen (δ^{18} O), and strontium (87Sr/86Sr) are critical in determining fluid properties and origins during carbonate diagenesis, enabling precise reconstruction of paleoenvironmental conditions, such as temperature, pressure, biological factors, salinity, redox potential, and pH values due to fractionation (Banner, 1995; Warren, 2000; Nasir et al., 2008; Dworczak et al., 2022). The isotopic characteristics of matrix rocks and cements were extensively documented in our previous study (Huang et al., 2022), though results may vary due to measurement limitations. To improve precision, we have combined whole-rock and in-situ isotope testing. The findings are as follows: (i) all samples exhibit Mn/Sr ratios (0.01-0.48), well below the range established by Kaufman et al. (1991), validating the isotopic data; (ii) matrix limestones, represented by ML and PS, display $\delta^{13}C_{VPDB}$ values between -1.1% and -0.6% (mean -0.9%) and $\delta^{18}O_{VPDB}$ values from -7.9% to -6.0% (mean -7.1%), with ML showing 87 Sr/ 86 Sr ratios of 0.70869–0.70897; (iii) RFC samples have δ^{13} C_{VPDB} values of 0.6%, $\delta^{18}O_{VPDB}$ values of -5.0%, and $^{87}Sr/^{86}Sr$ ratios from 0.70868 to 0.70882; (iv) $\delta^{18}O_{VPDB}$ values in C1 show a slight decrease (-9.7% to -8.9%), with more pronounced low values in C2 (-13.4% to -11.3%), C3 (-10.9% to -12.2%), and VC (-17.1% to -15.8%) (Fig. 6(a)); (v) 87 Sr/ 86 Sr ratios for C1, C2, and C3 range from 0.70861 to 0.70893 (mean 0.70877), 0.70850 to 0.70888 (mean 0.70864), and 0.70864 to 0.70918 (mean 0.70881), respectively; and (vi) VC displays the highest 87Sr/86Sr ratios among calcite cements, ranging from 0.70935 to 0.70939 (mean 0.70937) (Table 1).

4.2.2. Trace elements

Trace elements are incorporated into sedimentary matrices through processes such as co-precipitation or adsorption, appearing either as chemical precipitates or biological remnants (Frimmel, 2009; Meyer et al., 2012). The enrichment patterns, distribution characteristics, and elemental ratios of these trace elements, as documented by geochemical indicators, can provide crucial insights into the paleoclimate, paleoenvironment, and fluid sources active during the formation period (Tribovillard et al., 2006; Meyer et al.,

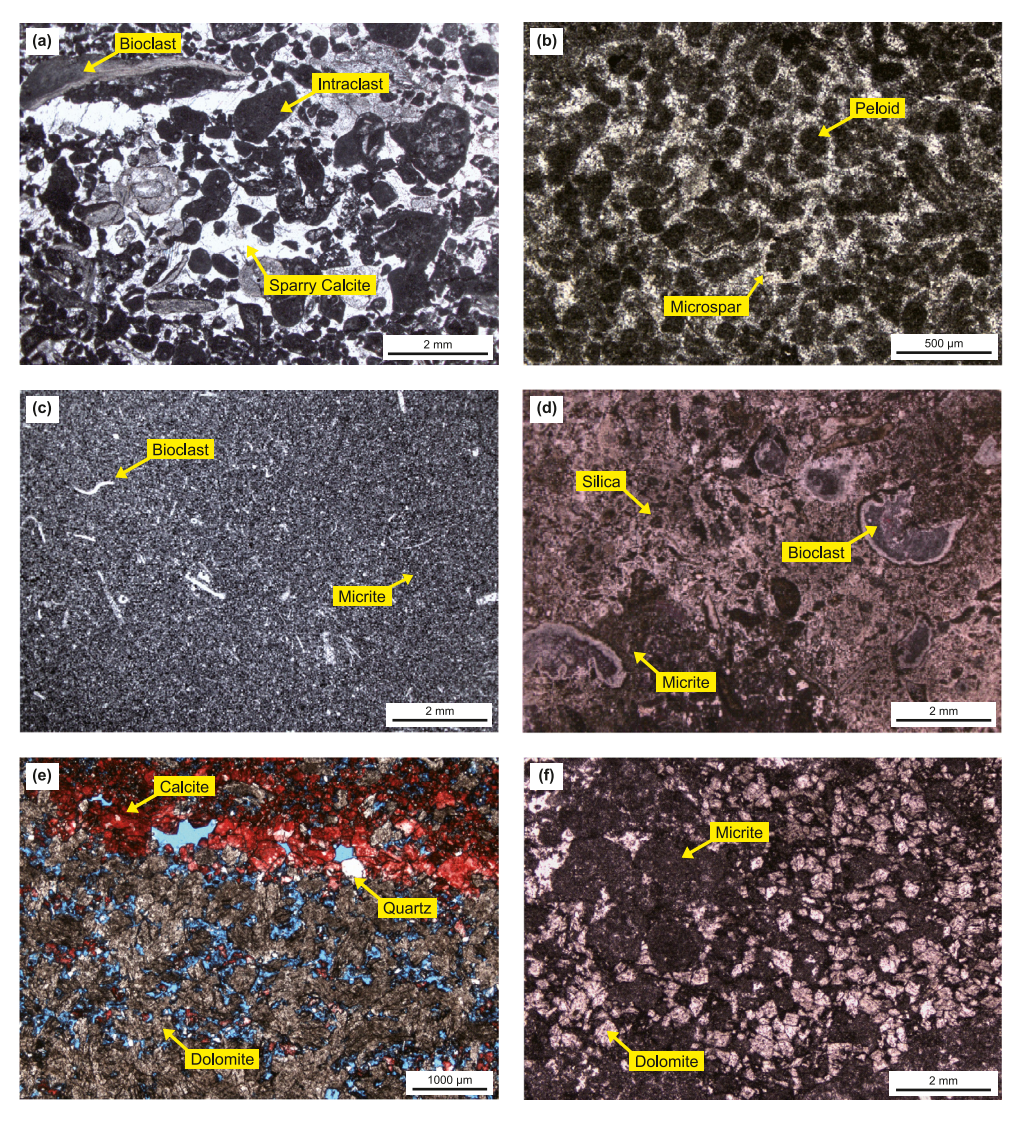


Fig. 2. Thin section photomicrographs of identified lithofacies. **(a)** Plane-polarized light image of GS. The main distinguishing features are the variations in particle composition and presence of sparry cement, SHB2, O₂yj, 7441.20 m; **(b)** Plane-polarized light image of PS. This sample exhibits a high density of spherical peloids and microspar crystals, SP1, 7778.81 m, O₂yj; **(c)** Plane-polarized light image of ML. Bioclasts are dispersed within the micrite matrix, SHB5, 7332.23 m, O₂yj; **(d)** Plane-polarized light image of SL. The presented sample exhibits a non-selective, patchy replacement of the ML by silica, SHB1-7, 7357.11 m, O₂yj; **(e)** Plane-polarized light image of DS. The intercrystalline pores are partially occupied by calcite, SHBP1, 8450.60 m, O₁₋₂y; **(f)** Plane-polarized light image of DL. SP2, 7534.10 m, O₁₋₂y.

2012; Robbins et al., 2016). In carbonate rocks, the concentrations, fractionation patterns, and anomalies of rare earth elements (REEs) reveal the properties of the original aqueous environment and offer significant insights into ancient marine conditions and mineral precipitation processes (Nothdurft et al., 2004; Herwartz et al., 2013; Kowal-Linka et al., 2014). To ensure robust conclusions, high-resolution sampling and careful mitigation of contamination or alteration by non-carbonate constituents (e.g. silicate minerals) are essential throughout sedimentation and dissolution phases before systematic analysis.

Individual LA spot elemental values (n = 25) are summarized in Tables 2 and 3. REY data presented as Post-Archean Australian Shale (PAAS)-normalized diagrams for different calcite cement generations, are shown in Fig. 7. Al, Zr, and Th show marked enrichment in siliciclastic material, making their concentrations reliable indicators of sample contamination (Nothdurft et al., 2004). Additionally, the correlation between Al contents, (Pr/Tm)_N ratios, and Σ REE concentrations yielded the following results: (i) all measured Al, Zr, and Th concentrations fall below the

contamination screening standards established by Frimmel (2009) (Al < 100 ppm; Zr < 4 ppm; Th < 0.1 ppm); (ii) Al content in ML is significantly higher than in all other cements, nearing 100 ppm; and (iii) no significant correlation is observed between Al contents and (Pr/Tm)_N ratios with Σ REE concentrations, as shown in Fig. 6(b). These results confirm that all cement samples remain uncontaminated, accurately representing their corresponding primordial fluids. However, the Al content in ML, close to the threshold, may indicate a significant proportion of clay minerals in the sample. Additionally, the Pr anomaly serves as a reliable indicator reflecting the Ce anomaly, consistent with previous studies by Bau and Dulski (1996) and Planavsky et al. (2010). The alignment of (Pr/Pr*)_N and (Ce/Ce*)_N values indicates that these samples exhibit true Ce anomalies, unaffected by La anomalies (Fig. 6(c)).

ML samples (n=3) exhibit high Sr contents (178.32 550.90 ppm) and notably low Mn contents (6.03–11.11 ppm), while the REY_{SN} shows a slightly negative Ce anomaly (0.78–0.98) and subtly convex profile patterns with BSI values ranging from 1.12 to 1.46.

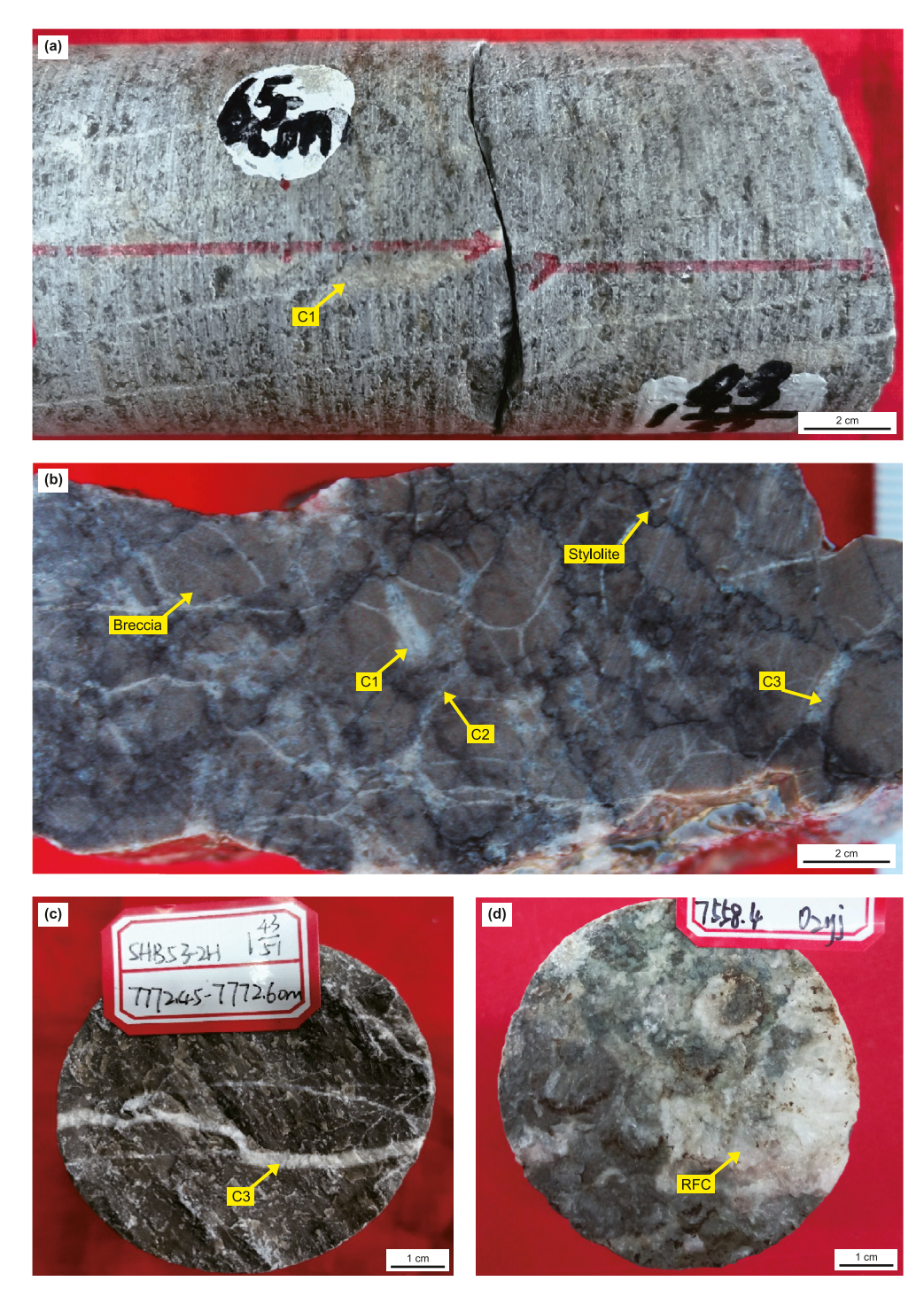


Fig. 3. Petrographic characteristics of calcite cements. **(a)** Photograph of C1. The high angle fractures of WS are uniformly filled with C1, SHB5, 7426.49–7426.55 m, O₂yj; **(b)** Photograph of intercut calcite veins. The ML is fractured into breccia, which is infilled with C1, C2, and C3 minerals between the fragments, and intersected by intricate stylolite structures, SHB52, 7425.00–7425.20 m, O₂yj; **(c)** Photograph of C3. The high angle fractures of ML are filled with C3, SHB53, 7772.45–7772.60 m, O₂yj; **(d)** Photograph of RFC. The RFC fills the fractures and pores of ML, appearing as white patches on the cross section of the core, SHB51, 7558.40–7558.50 m, O₂yj.

RFC (n=2) exhibits high Sr contents (206.44–418.20 ppm), Mn contents (14.40–24.16 ppm), and the lowest Σ REE concentrations (0.17–0.69 ppm), showing a distinctly negative Ce anomaly (0.14–0.17), depleted LREEs, and elevated Y/Ho ratios of 45.9–55.8. C1 (n=3) displays a REY_{SN} pattern similar to RFC but with a mildly negative Ce anomaly (0.61–0.74), the highest Mn and Fe contents (40.70–68.35 ppm and 562.08–1500.00 ppm, respectively), and Σ REE concentrations from 5.51 to 17.88 ppm. C2 (n=6) shows

slightly different REY_{SN} patterns from C1, with mildly convex profiles, BSI values from 1.06 to 1.62, lower Σ REE concentrations (0.02–0.12 ppm), and Y/Ho ratios of 26.72–54.51. The REY_{SN} patterns observed in C3 (n=7) are notably flat, with the lowest Y/Ho ratios (21.30–32.09). Finally, VC (n=4) is characterized by slightly positive Eu anomalies (1.05–1.36), high Σ REE concentrations (1.43–6.74 ppm), and decreased Y/Ho ratios (22.89–25.61) (Figs. 6 and 7).

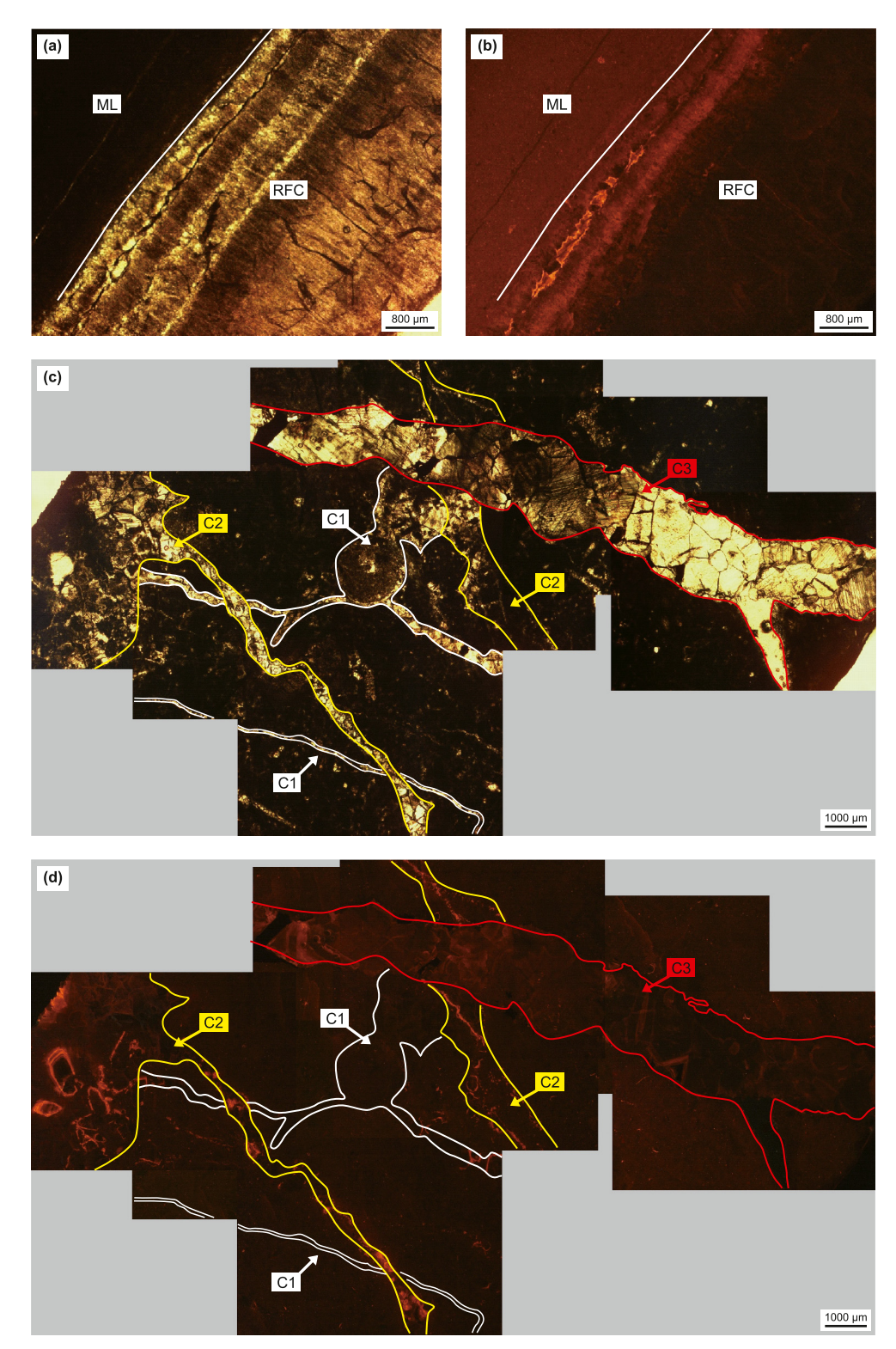


Fig. 4. Petrographic characteristics of calcite cements. **(a)** Photograph of RFC. The manifestation presents itself as unique isopachous cortices, SHB51, O₂yj, 7558.40 m; **(b)** Cathodoluminescence image of figure (a). The sample emits a faint luminosity; **(c)** The captivating image shows the intercutting phenomenon with C1, C2, and C3 under the influence of plane-polarized light, SHB52, 7425.00 m, O₂yj; **(d)** Cathodoluminescence image of figure (c). The cements exhibit a consistent, mottled appearance with a dull red light respectively.

4.2.3. U-Pb dating

In recent years, U-Pb chronology has emerged as a powerful tool to unravel the evolutionary history of carbonate bodies. However, it has inherent limitations: (i) strong heterogeneity resulting from multi-phase fluid activity events presents challenges in ensuring

the accuracy of calcite ages (Roberts and Waker, 2016); (ii) appropriateness of the standard sample (Elisha et al., 2021); (iii) the open or closed state of the U-Pb system (Smye et al., 2018); and (iv) low U content coupled with high common Pb content can complicate analysis efforts (Rasbury et al., 2021). To mitigate these issues, this

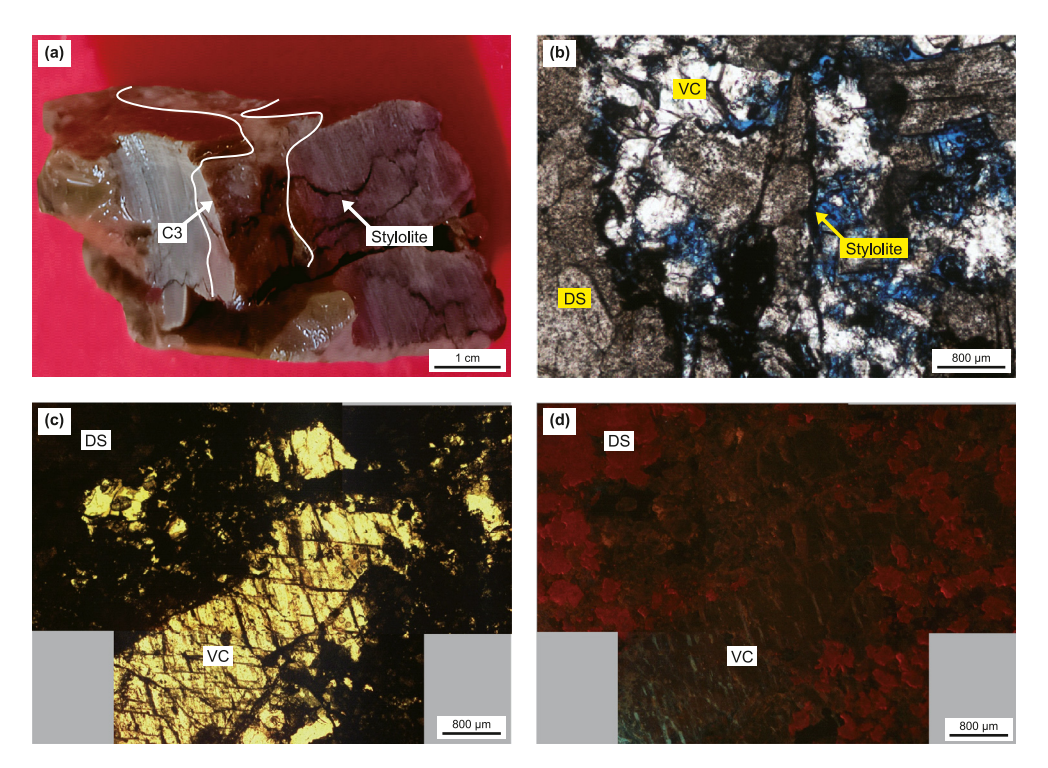


Fig. 5. Petrographic characteristics of calcite cements. **(a)** Core sample of C3, SHB7, O₁₋₂y, 7729.85 m; **(b)** The image shows pores filled with VC and intersected by stylolite under plane-polarized light, SHBP1, O₁₋₂y, 8450.60 m; **(c)** The image depicts plane-polarized light revealing VC filling in the pore of DS, SHBP1, O₁₋₂y, 8451.20 m; **(d)** Cathodoluminescence image of figure (c). The VC shows consistently dull light.

study employed electron cathode luminescence imaging to distinguish different generations of calcite. Additionally, advanced LA-ICP-MS dating techniques were used to enhance sensitivity and spatial resolution, selecting the international standard sample AHX-1d for comparative analysis purposes. Finally, precise corrections were applied using the Tera-Wasserburg harmonic curve method to minimize potential inaccuracies due to system opening during measurements. As a result of these methodological refinements, two C3 samples obtained from fault zones Nos. 5 and 7 were analyzed with exceptional precision, yielding isochron ages of 464 ± 21 Ma and 461.9 ± 5.0 Ma, respectively (Fig. 8).

5. Discussion

5.1. Paragenetic sequence

Petrographic relationships, coupled with geochemical data and U-Pb isotopic dating, elucidate the spatial-temporal succession of diagenetic processes. This progression can be visualized as follows: as particles and micrites accumulate on the seabed and enter the burial environment, the RFC is distributed along the interior of original fracture and pore walls, representing the earliest generation of calcite cement. Subsequently, C1, C2, and C3 formed successively within multi-stage fractures that likely did not form at significant burial depths due to intersecting stylolites. Following this sequence, dolomites with a planar-s to planar-e crystal habit precipitated along these stylolites. Variations in dolomitized fluid flow within the burial environment led to partial transformation of DL into DS, with an approximate thickness of 0.1 m. DS occurrence is limited to section 8450.60-8450.70 m in well SHBP1 and is absent in other wells. Furthermore, this interval shows dense stylolite distribution without supporting mineralogical or geochemical evidence for dolomite, suggesting local dolomitization during compaction flow events (Machel, 2004). Lastly, VC and minor

quartz precipitated within DS pores, signifying the final two generations (Fig. 9).

5.2. Fluid sources accountable for multi-stage cementation

5.2.1. Calcite generated in submarine diagenetic environment

The isotopic values of ML fall within δ^{13} C (-2.0%-0.5%), δ^{18} O (-8.0% to -4.5%), and $^{87}\text{Sr}/^{86}\text{Sr}$ (0.7085–0.7090), consistent with Early-Middle Ordovician marine calcite as reported by Veizer et al. (1999) (Fig. 6(a) and (d)). In conjunction with our previous findings (Huang et al., 2022), this suggests the host rock originated in the primordial ocean during this period (Tucker and Wright, 1990). Despite possible diagenetic alteration, the REY_{SN} patterns are imperfect (Fig. 7), yet they remain useful for comparative analysis. The RFC's isopachous crustal geometry with weak cathode luminescence also supports its identification as submarine cement (Longman, 1980; Kendall and Tucker, 2010) (Fig. 4(a) and (b)). This interpretation is further reinforced by geochemical indicators: (i) Machel (2004) suggested that δ^{13} C fractionation is unlikely to occur solely due to temperature and pressure variations, whereas δ^{18} O is highly sensitive to changes in temperature and salinity. Thus, the significant $\delta^{13}C$ and $\delta^{18}O$ disparity between the host rock and RFC suggests nonconsecutive formation processes; (ii) the REY_{SN} pattern and ΣREE concentrations are effective for tracking fluid sources, redox states, and paleoclimate (Lottermoser, 1992; De Carlo and Green, 2002; Tostevin et al., 2016). RFC's REY_{SN} patterns resemble seawater proxies, exhibiting a standard Y/Ho value and a pronounced negative Ce anomaly (Fig. 7(a)), which may indicate elevated dissolved oxygen levels in seawater column (Tachikawa et al., 1999). Low SREE concentrations imply that RFC precipitated just below the sediment-water interface in a shallow marine environment (Planavsky et al., 2010); and (iii) consensus supports a primary origin for these cements alongside precursor calcite

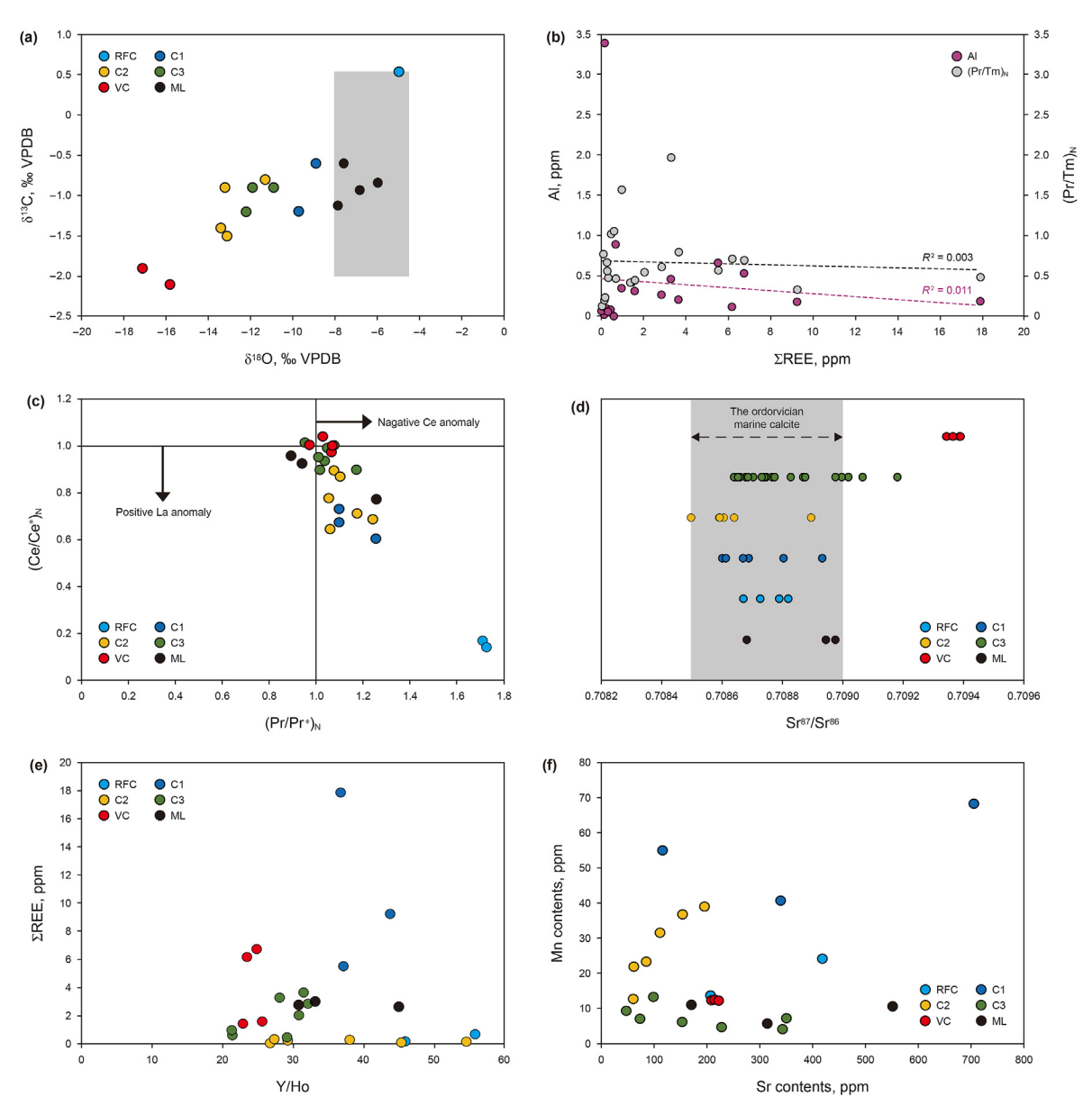


Fig. 6. (a) Cross plot of δ^{13} C and δ^{18} O values of samples, with the Lower-Middle Ordovician marine calcite range represented by the grey area (Veizer et al., 1999); (b) Plots of Al contents and (Pr/Tm)_N ratios versus ΣREE concentrations, showing all negative correlation; (c) The diagram discriminating between La and Ce anomalies (after Bau and Alexander, 2009); (d) The ⁸⁷Sr/⁸⁶Sr ratios of samples. The ⁸⁷Sr/⁸⁶Sr range of the Lower-Middle Ordovician marine calcite, indicated by the grey area, are sourced from Veizer et al. (1999); (e) ΣREE concentration and Y/Ho ratios. The dashed lines show the range of Y/Ho empirical values for seawater and meteoric water (Bolhar and Van Kranendonk, 2007; Su et al., 2022); (f) The scatter diagrams of Mn and Sr contents.

mineralogy (Arthur, 1986; Woo and Anders, 1993; Mazzullo et al., 2010; Kendall and Tucker, 2010). Although no experimental samples definitively confirm this origin, if RFC formed via replacement, high-magnesium calcite is the likely precursor mineral rather than aragonite due to its low Sr content and distinct crystal habit (Lambert et al., 2006; Kendall and Tucker, 2010).

5.2.2. Calcite derived from the connate seawater preserved in the host limestone

Typical burial environment calcite characteristics include Sr and $\delta^{18}\text{O}$ depletion with Mn and Fe enrichment (Brand and Veizer, 1980; Bau et al., 2010; Bartley et al., 2001). Given the relatively diminished presence of interfering components, it is imperative to use the previously published whole-rock $\delta^{18}\text{O}$ data by Huang et al. (2022)

as a crucial point of reference, showcasing a subtle depletion. Examination of Mn and Fe contents, ⁸⁷Sr/⁸⁶Sr values, and Y/Ho ratios suggests C1 formation followed RFC precipitation during the burial stage (Fig. 6(d), (e) and (f)). During this stage, ΣREE concentrations increase, shifting the REY_{SN} pattern from seawater-type to a shale-normalized pattern enriched in LREEs and MREEs due to deeper diagenetic influence (Elderfield and Sholkovitz, 1987; Bayon et al., 2011). Consequently, C1 likely precipitated early in this stage with minimal oxidation (Fig. 7(b)), involving partial iron (oxy) hydroxide dissolution and unstable sediment decomposition, elevating Fe and ΣREE concentrations (Hannigan and Sholkovitz, 2001; Haley et al., 2004; Bayon et al., 2011). Given C1's position within the sample, its precipitation likely occurred during the eogenetic stage, initiated by connate seawater activation in the host limestone during a tectonic event.

Table 1 C-O-Sr isotopic compositions of limestones and calcite cements (the data indicated by the asterisk is sourced from Huang et al., 2022).

Well No.	Mineral	Method	δ^{13} C(‰VPDB)	$\delta^{18}O(\text{‰VPDB})$	⁸⁷ Sr/ ⁸⁶ Sr	Sample/laser-spot
SHBP2H	ML	Whole-rock	-0.8	-6.0	_	1
SHB7	ML	Whole-rock	-1.1	-7.9	_	1
SHB7	PS	Whole-rock	-0.9	-6.8	_	1
SHB11	ML	Whole-rock/in-situ	-0.6	-7.6	0.70869-0.70897	1/3
SHB51X	RFC	In-situ	0.5	-5.0	0.70868-0.70882	4
YJ1X	C1	In-situ	_	_	0.70861-0.70893	7
SHB1	C1	Whole-rock	-0.6	-8.9	_	1
SHB1	C1	Whole-rock	-1.2	-9.7	_	1
SHB52A	C2	In-situ	_	_	0.70859-0.70864	4
SHB1	C2	Whole-rock	-1.5*	-13.1*	_	1
SHB2	C2	Whole-rock	-1.4*	-13.4*	_	1
SHB7	C2	Whole-rock	-0.9*	-13.2*	0.70888*	1
SHBP3H	C2	Whole-rock	-0.8*	-11.3*	0.70850*	1
SHB52A	C3	In-situ	_	_	0.70907-0.70918	2
SHB7	C3	In-situ	_	_	0.70798-0.70888	11
YJ1X	C3	In-situ	_	_	0.70865-0.70902	5
SHBP2H	C3	In-situ	_	_	0.70864-0.70898	6
SHB1	C3	Whole-rock	-0.9*	-11.9*	_	1
SHB1	C3	Whole-rock	-0.9*	-10.9*	_	1
SHB1	C3	Whole-rock	-1.2*	-12.2*	0.70879*	1
SHBP1	VC	In-situ	_	_	0.70935-0.70939	4
SHB1	VC	Whole-rock	-1.9*	-17.1*	_	1
SHBP3H	VC	Whole-rock	-2.1*	-15.8*	_	1

 Table 2

 REY concentrations (ppm) of matrix rocks and calcite cements.

Mineral	Spot	La	Ce	Pr	Nd	Sm	Eu	Gd	Tb	Dy	Y	Но	Er	Tm	Yb	Lu	REE
ML ML ML	SHB5-1-1 SHB7-1-1 SHB7-1-2	0.638 0.575 0.609	1.216 1.004 1.119	0.144 0.152 0.114	0.653 0.497 0.532	0.120 0.083 0.064	0.022 0.015 0.012	0.128 0.132 0.067	0.016 0.009 0.008	0.084 0.072 0.071	0.620 0.580 0.405	0.019 0.013 0.013	0.038 0.033 0.034	0.006 0.007 0.004	0.032 0.024 0.025	0.004 0.002 0.002	3.12 2.62 2.67
RFC RFC	SHB51-1-1 SHB51-1-2	0.062 0.239	0.016 0.059	0.007 0.038	0.025 0.146	0.008 0.036	0.002 0.008	0.012 0.039	0.001 0.006	0.009 0.040	0.184 0.549	0.004 0.010	0.011 0.032	0.001 0.004	0.011 0.025	0.002 0.004	0.17 0.69
C1 C1 C1	SHB52A-1-2 SHB52A-1-4 YJ1X-1-5	1.396 1.498 2.930	1.738 2.523 4.600	0.249 0.420 1.010	1.005 1.861 4.220	0.184 0.478 0.960	0.053 0.109 0.231	0.235 0.602 0.980	0.035 0.092 0.171	0.234 0.621 1.080	1.990 6.443 8.300	0.054 0.147 0.226	0.156 0.429 0.660	0.020 0.058 0.095	0.134 0.350 0.620	0.021 0.052 0.092	5.51 9.24 17.88
C2 C2 C2 C2 C2 C2 C2	SHB52A-1-6 SHB52A-1-7 SHB7-4-2 SHB7-4-6 YJ1X-4-4 SHB11-1-2	0.007 0.040 0.026 0.028 0.001 0.021	0.028 0.077 0.082 0.094 0.007 0.026	0.008 0.015 0.015 0.017 0.002 0.004	0.035 0.064 0.069 0.079 0.009 0.019	0.010 0.014 0.011 0.022 0.002 0.006	0.003 0.004 0.003 0.004 0.000 0.001	0.015 0.019 0.017 0.029 0.004 0.005	0.003 0.003 0.002 0.003 0.001 0.001	0.014 0.019 0.015 0.020 0.004 0.005	0.118 0.155 0.091 0.128 0.035 0.040	0.002 0.004 0.003 0.005 0.001 0.001	0.011 0.012 0.009 0.014 0.003 0.003	0.002 0.001 0.001 0.002 0.001 0.000	0.009 0.006 0.007 0.011 0.002 0.003	0.002 0.001 0.001 0.002 0.000 0.000	0.15 0.28 0.26 0.33 0.04 0.10
G G G G G G	SHB-7-2-2 SHB-7-2-4 SHB-7-2-5 SHB-7-2-6 YJ1X-4-7 YJ1X-5-4 SHB7-1-3	0.285 0.934 0.809 0.153 0.440 0.227 0.061	0.738 1.463 1.522 0.264 1.106 0.434 0.171	0.099 0.146 0.167 0.027 0.143 0.042 0.028	0.412 0.480 0.626 0.089 0.549 0.157 0.112	0.101 0.074 0.121 0.017 0.134 0.023 0.024	0.018 0.010 0.019 0.003 0.026 0.005 0.004	0.097 0.067 0.105 0.013 0.131 0.025 0.020	0.017 0.007 0.017 0.003 0.020 0.002 0.003	0.108 0.043 0.104 0.011 0.115 0.021 0.018	0.644 0.239 0.708 0.063 0.799 0.088 0.107	0.021 0.009 0.022 0.003 0.025 0.004 0.004	0.063 0.026 0.063 0.009 0.070 0.011 0.010	0.008 0.003 0.010 0.001 0.011 0.001 0.001	0.061 0.023 0.057 0.007 0.066 0.010 0.007	0.007 0.004 0.007 0.001 0.010 0.001 0.001	2.04 3.29 3.65 0.60 2.85 0.96 0.46
VC VC VC	SHBP1-N1-1 SHBP1-N1-2 SHBP1-N1-7 SHBP1-N1-8	0.790 0.203 0.158 0.962	2.320 0.544 0.477 2.492	0.312 0.073 0.069 0.345	1.342 0.347 0.294 1.427	0.344 0.084 0.079 0.361	0.075 0.022 0.018 0.083	0.283 0.082 0.090 0.324	0.042 0.011 0.014 0.046	0.279 0.083 0.083 0.288	1.284 0.420 0.424 1.416	0.055 0.016 0.019 0.057	0.146 0.051 0.052 0.153	0.020 0.007 0.008 0.023	0.139 0.055 0.060 0.154	0.022 0.009 0.009 0.022	6.17 1.59 1.43 6.74

5.2.3. Calcites related to meteoric water intrusion

To confirm the meteoric water origin of calcite cement, several well-established criteria exist: (i) despite the inherent scarcity of dissolved ions in meteoric water, water-rock reactions resulting from deep seepage can give rise to calcite exhibiting elevated Fe and Mn contents, as well as diminished Sr levels, within specific open geological settings (Kaufman and Knoll, 1995); (ii) the extensive range of δ^{18} O values may easily be misinterpreted as having alternative origins, yet the coexistent trend between δ^{13} C

and $\delta^{18}O$ values can serve as an exceptionally effective point of reference (Nan and Liu, 2004); (iii) depleted REE concentration as a result of low temperature (Zhao et al., 2019); (iv) a flatter REY_SN pattern (Bolhar and Van Kranendonk, 2007); and (v) low salinity with almost zero salt content, indicating an ice final melting temperature close to 0 °C in fluid inclusions (Goldstein, 2001).

In light of the abundance of data and practical circumstances at hand, we contend that the C2, C3, and VC are likely to have originated from meteoric sources with distinct characteristics, for the

Table 3Trace elemental concentrations (ppm) and REY parameters of calcite cements.

Mineral	Spot	Al	Zr	Th	Fe	Mn	Sr	Mn/Sr	(Eu/Eu*) _N	(Ce/Ce*) _N	(Pr/Pr*) _N	BSI	Y/Ho	(Pr/Tm) _N
ML	SHB5-1-1	84.43	0.02	0.02	303.33	11.11	178.32	0.06	0.97	0.93	0.94	1.44	33.12	1.05
ML	SHB7-1-1	95.28	0.16	0.03	334.31	6.03	315.16	0.02	1.01	0.78	1.26	1.46	45.98	1.01
ML	SHB7-1-2	81.24	0.23	0.10	580.73	10.24	550.90	0.02	1.00	0.98	0.87	1.12	31.15	1.31
RFC	SHB51-1-1	3.38	0.18	_	577.68	24.16	418.16	0.06	1.13	0.17	1.71	0.77	45.85	0.24
RFC	SHB51-1-2	0.89	0.19	_	883.76	14.40	206.44	0.07	1.10	0.14	1.72	1.07	55.77	0.47
C1	SHB52A-1-2	0.67	0.01	0.03	605.49	54.98	115.69	0.48	1.31	0.67	1.10	1.08	37.11	0.57
C1	SHB52A-1-4	0.18	0.04	3.50×10^{-3}	562.08	68.35	104.73	0.10	1.04	0.73	1.10	1.26	43.73	0.33
C1	YJ1X-1-5	0.19	0.04	4.30×10^{-3}	1500.00	40.70	339.00	0.12	1.13	0.61	1.26	1.24	36.73	0.49
C2	SHB52A-1-6	0.02	5.57×10 ⁻⁵	3.00×10^{-3}	557.75	36.81	153.60	0.24	1.21	0.69	1.24	1.21	54.51	0.20
C2	SHB52A-1-7	0.09	1.19×10^{-4}	_	644.35	31.57	111.00	0.28	1.40	0.71	1.17	1.52	38.00	0.56
C2	SHB7-4-2	0.10	3.28×10^{-3}	_	555.85	21.92	61.32	0.36	1.33	0.87	1.10	1.35	29.21	0.67
C2	SHB7-4-6	0.06	5.69×10^{-5}	3.20×10^{-3}	1092.98	12.69	60.34	0.21	0.87	0.90	1.08	1.62	27.33	0.48
C2	YJ1X-4-4	0.07	1.70×10^{-3}	5.34×10^{-7}	486.00	39.00	195.00	0.20	0.91	0.78	1.05	1.07	26.72	0.13
C2	SHB11-1-2	0.12	1.16×10^{-3}	4.20×10^{-3}	678.73	23.35	84.87	0.28	0.95	0.65	1.06	1.52	45.32	0.77
C3	SHB-7-2-2		_	0.01	411.01	4.11	342.83	0.01	0.87	0.99	1.05	1.35	30.81	0.55
C3	SHB-7-2-4	0.46	0.02	0.01	415.26	6.18	152.81	0.04	0.73	0.90	1.02	0.92	28.07	1.96
C3	SHB-7-2-5	0.21	0.02	0.07	425.52	4.69	227.39	0.02	0.80	0.95	1.01	1.09	31.48	0.80
C3	SHB-7-2-6	0.01	0.01	0.07	585.81	9.32	46.95	0.20	0.93	0.94	1.04	0.89	21.39	1.05
C3	YJ1X-4-7	0.27	0.04	0.03	359.00	7.21	350.00	0.02	0.97	1.00	1.08	1.31	32.09	0.61
C3	YJ1X-5-4	0.35	0.03	0.01	437.39	7.07	73.30	0.10	1.20	1.02	0.95	1.06	21.30	1.57
C3	SHB7-1-3	0.09	2.60×10^{-3}	7.95×10^{-9}	517.61	13.28	98.64	0.13	0.99	0.90	1.17	1.42	29.13	1.02
VC	SHBP1-N1-1	0.12	_	0.10	536.36	12.52	219.92	0.06	1.17	1.04	1.03	1.46	23.45	0.71
VC	SHBP1-N1-2	0.32	_	0.02	529.50	12.34	208.21	0.06	1.36	1.01	0.97	1.27	25.61	0.45
VC	SHBP1-N1-7	0.42	_	0.01	478.16	12.26	222.08	0.06	1.05	1.00	1.07	1.30	22.89	0.42
VC	SHBP1-N1-8	0.54	1.30×10^{-3}	0.08	489.72	12.36	216.13	0.06	1.22	0.98	1.06	1.46	24.83	0.70

following reasons: (i) the determination of the covariant relationship between $\delta^{13}C$ and $\delta^{18}O$ values cannot be made arbitrarily due to the limited number of samples, but the presence of conspicuous depletions and significant disparity in the δ^{18} O values can serve as a robust foundation for judgment (Fig. 6(a)); (ii) our previous study (Lu et al., 2020) has established precise ice final melting temperatures (T_{m-ice}) of primary fluid inclusions under rigorous constraints of fluid inclusion petrology and FIA analysis (C3 and VC typically ranging from -0.4 to -0.2 °C) (Fig. 10). These marginally lower values may be attributed to potential re-equilibration of fluid inclusions, or to the intermingling of meteoric water and pore water; (iii) the features of low Σ REE concentrations, flat and slightly convex REY_{SN} profiles, and low Y/Ho ratios (Figs. 6 and 7) bear resemblance to the meteoric calcite cement documented by predecessors (Bolhar and Van Kranendonk, 2007; Su et al., 2022); (iv) the ⁸⁷Sr/⁸⁶Sr ratios and SREE concentrations exhibit a bimodal distribution. C2 and C3 demonstrated similar values, whereas VC displayed notably higher values (Fig. 6(d) and (e)). This differentiation aligns with the diagenetic sequence associated with dolomitization events. (v) The isochron ages of the C3 cluster are approximately 462-464 Ma (Fig. 8), indicating that C2 and C3 were both formed during the eogenetic stage influenced by the first episode of the Middle Caledonian movement. The primary factor contributing to the absence of a significant increase in Fe and Mn content within the calcites, contrary to empirical expectations, may lie in the insufficiency of water-rock reaction processes (Fig. 6(f)), and (vi) the occurrence of the third episode of the Middle Caledonian movement followed the deposition of thick Upper Ordovician clastic rocks in the SHB. During this period, the emergence of new faults, cutting through, and leaching clastic rocks with meteoric water could have resulted in a discernible increase in the 87Sr/86Sr ratio and Eu anomaly in the calcite (Nozaki et al., 2000). Consequently, this phenomenon provides a compelling explanation for the development of VC.

5.2.4. Reassessment of hydrothermal activity

The previously reported calcite origin was fully ascertained by

analyzing whole-rock isotopes and trace elements (Huang et al., 2022). These geochemical signals may be subject to potential effects from clay impurities or other minerals, thus posing challenges in accurately discriminating fluid flow within the rock record. Fortunately, we could promptly rectify the initial 'hydrothermal' interpretation and instead rely on in-situ isotope analysis, REY examination, and fluid inclusions investigation as more reliable indicators at present. The carbonate mineral formed by hydrothermal fluids typically exhibit distinct positive Eu anomaly, elevated ΣREE concentration, LREE-enriched profile, and indications of high temperature and salinity (Cathles and Smith, 1983; Franchi et al., 2015; Sylvestre et al., 2017). However, based on the aforementioned discussion, it becomes abundantly clear that the preponderance of calcite as the primary constituent mineral in rock formation unequivocally indicates extensive hydrothermal activity during the protracted sedimentary tectonic evolution of SHB is highly improbable. Quartz is one of the most important mineral types resulting from thermal events and involves either the cooling of dissolved silicon dioxide in hydrothermal fluids or a decrease in pressure, leading to the precipitation of amorphous opals. Subsequently, recrystallisation gives rise to microcrystalline or granular quartz, providing compelling evidence for the existence of hydrothermal activity in the SLU (Jiao, 2017; Wang, 2022). However, our on-site investigations reveal that macroscopically visible quartz components within the entire SHB were limited to adjacent wells (SHB1-7 and SHB2), with a thickness less than 0.5 m. These components appear as SL and quartz cement (Fig. 2(d) and (e)). Microscopic examination shows radial chalcedony, microcrystalline quartz, and opal along with numerous fluid inclusions observed in siliceous sections—an indication of rapid crystallization behavior driven by supersaturated solutions under varying environment condition (Rikke et al., 2010; Worden et al., 2012). The presence of residual carbonate matter, absence of silicon-based organisms (such as sponge spicules), and lack of volcanic minerals suggest that the SL may have formed through replacement involving silica-rich fluids. Furthermore, there have been reports on the REEs,

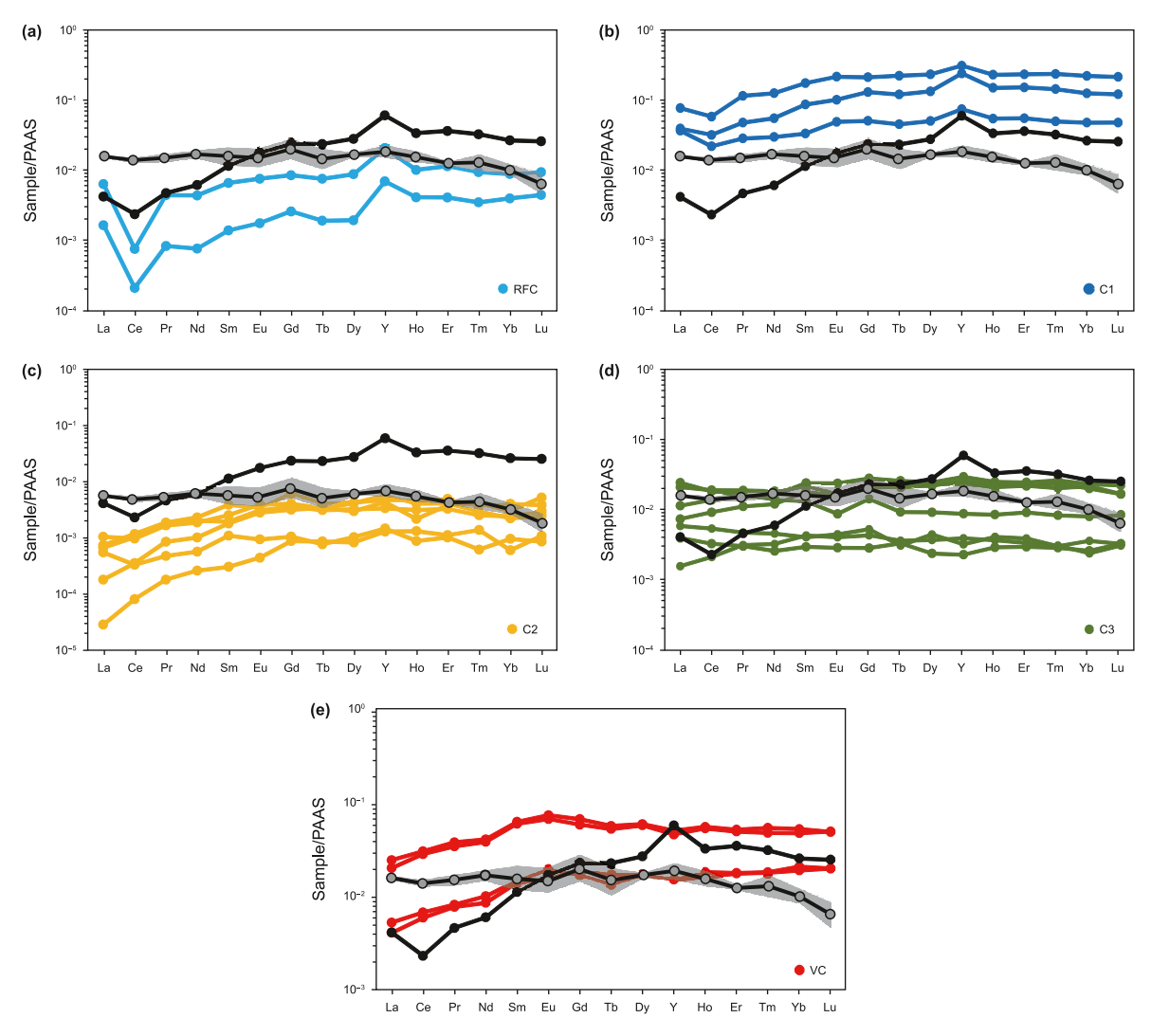


Fig. 7. PAAS-normalized REY patterns of all samples. The black curve represents the REY_{SN} pattern of modern Bahama ooids (Li et al., 2019), while the grey area illustrates the REY_{SN} pattern of matrix rocks (ML) with its inner line indicating the mean value of these samples.

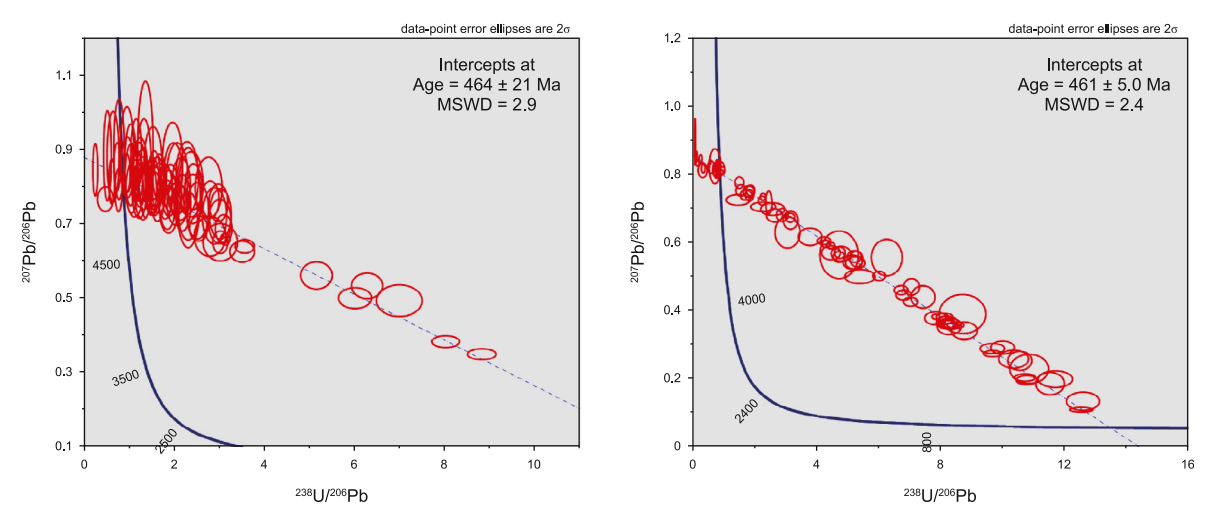


Fig. 8. Tera-Wasserburg concordia plots showing ²³⁸U/²⁰⁶Pb versus ²⁰⁷Pb/²⁰⁶Pb of C3.

particularly highlighting a positive Eu anomaly, as well as isotopic analyses indicating lower $\delta^{30}\text{Si}$ values. These findings suggest that

the fluid in question was indeed a true hydrothermal fluid, as supported by Wang et al. (2023). However, the siliceous

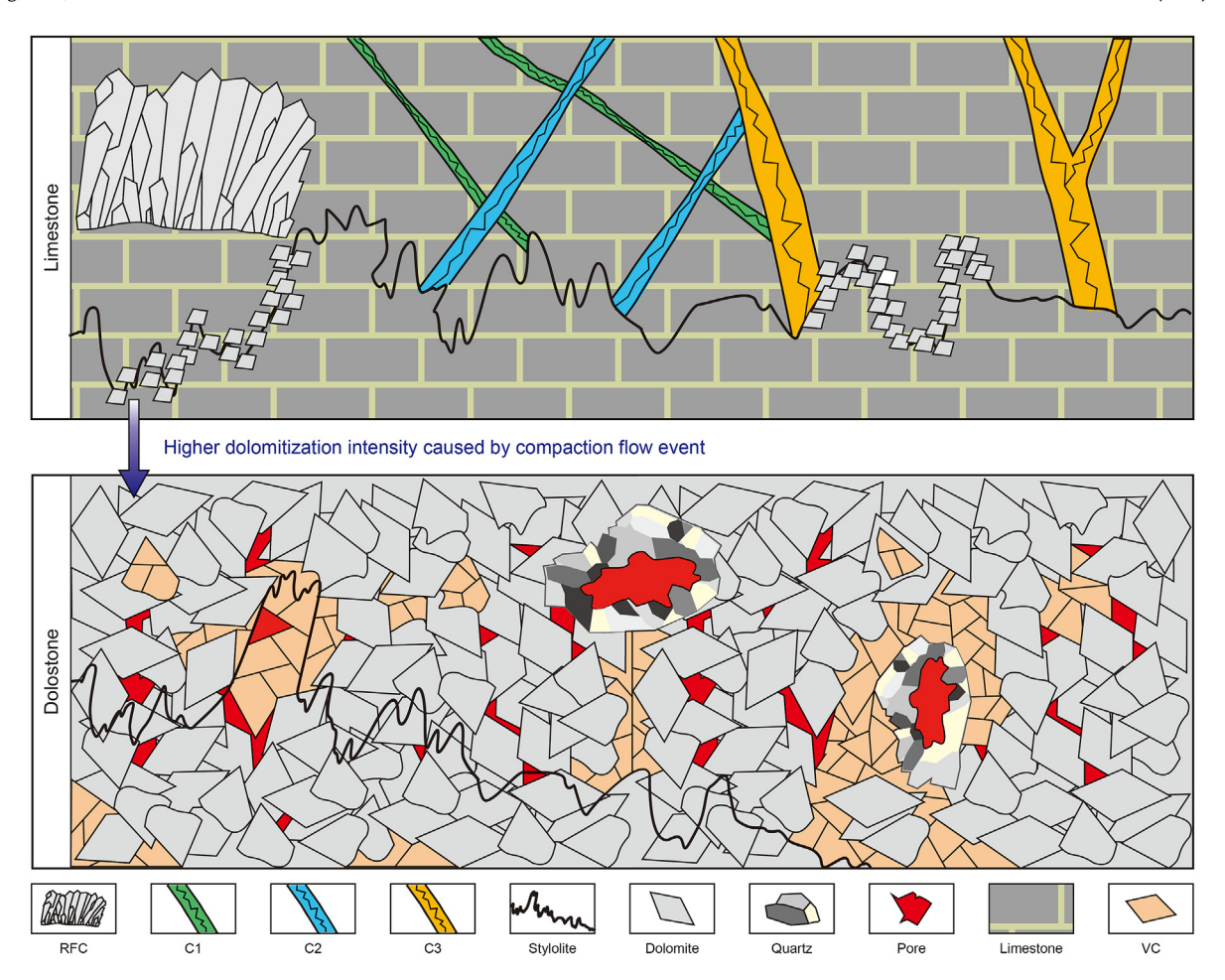


Fig. 9. A sketch illustrating the paragenesis sequence and cross-cutting relationships among diagenetic minerals.

components present in our specific sample were of such minuscule sizes that direct observation of fluid inclusions of primary or secondary origin was not feasible. This limitation poses a challenge when attempting to make an unequivocal 'hydrothermal' judgment based solely on direct observations. Therefore, any conclusions drawn regarding past thermal conditions remain speculative. This situation highlights an ongoing challenge in geothermal studies: while geochemical markers provide valuable insights into fluid origins and properties, their interpretation must be approached with caution when critical physical evidence, such as measurable temperatures, is lacking. Future research may benefit from exploring alternative methodologies or technologies that could enhance our ability to analyze minute quantities of materials more effectively or identify new proxies for assessing historical thermal regimes associated with hydrothermal systems. However, regardless of our acceptance of their viewpoint, we cannot disregard the crucial issue of the proportion of siliceous components within rocks. Therefore, the possibility of hydrothermal intrusion during burial must be considered. However, detection was limited to the plane range between the two aforementioned wells regardless of their origin. Notably, their macroscopic flow rate undoubtedly pales in comparison to meteoric water and formation water (e.g. connate seawater).

The SN, located in the southern region of the SLU, presents a distinct contrast as it has experienced a remarkable phase of vigorous hydrothermal activity. Evidence includes elevated geothermal gradients, extensive siliceous rocks and quartz

cements, calcite exhibiting a 'hydrothermal-REY_{SN} pattern', and mineral assemblages containing hornblende, potash feldspar, and fluorite (Li et al., 2015; Lu et al., 2017; Ye et al., 2022). By analyzing calcite fluid inclusions and conducting U-Pb dating, the timing of hydrothermal fluid activity in the SN has been confirmed as representing a third episode during the Middle Caledonian period and extending from the late Caledonian to the early Hercynian periods (Lu et al., 2017; Song et al., 2022). In terms of temporal factors, the potential for hydrothermal dispersion in SHB exists; however, spatially, despite the influence of subsequent thermal events, SHB can only represent the northernmost boundary of hydrothermal fluid migration from SN. This is due to SHB's comparable or greater number of strike-slip faults cutting through the Cambrian strata relative to SN (Han et al., 2023).

5.3. Model of fluid flows controlled by tectonic movements

This study proposes a phenomenological diagenetic model to explain fluid flow mechanisms: following rapid cementation of RFC and C1 within primary pores of carbonate sediments due to marine fluid influences (in seabed and shallow burial settings), a combination of compressional tectonics and sea-level decline results in meteoric water dominance during later diagenetic processes. Three possible scenarios for meteoric water migration are: (i) gravitational migration into the basin through permeable layers of the exposed orogenic belt; (ii) movement through the paleo-karst system along the fault zone; and (iii) direct infiltration along

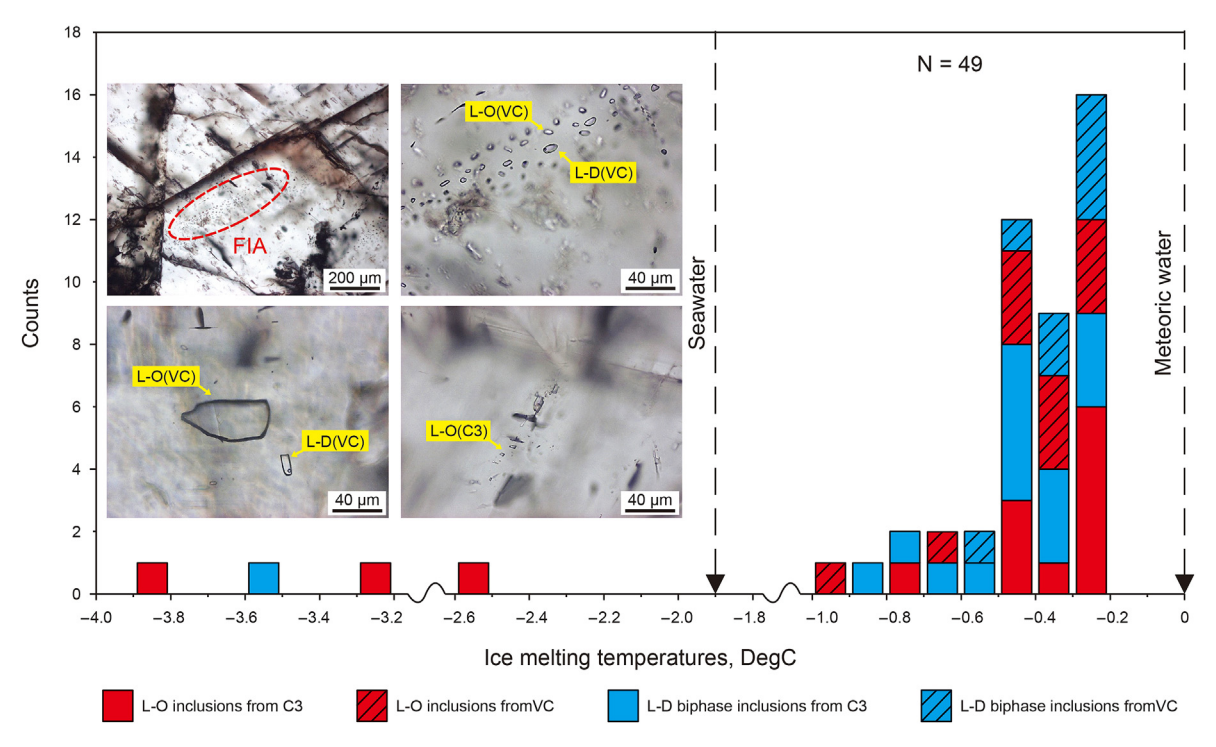


Fig. 10. Petrographic characteristics and histograms of ice-melting temperatures of fluid inclusions in C3 and VC (modified from Lu et al., 2020).

faults at the distal margin of the orogenic belt. The application of the first and second scenarios to SHB is challenging due to several factors: (i) the fluid hydraulic head, post-orogenic activity, influences only a limited area (up to 200 km) (Machel et al., 2002), much smaller than the linear distance between the Altyn orogenic belt and SHB; (ii) the closest paleo-karst lies in the northern basin, where meteoric water may penetrate deeply along the fault zone, the presumed primary diagenetic fluid pathway in the Ordovician formation (Chen et al., 2016; Lv et al., 2021). However, SHB's Ordovician carbonate strata are relatively flat, limiting the hydrodynamic potential for large-scale migration, leading to an unsupported 'fluid retention effect'. Furthermore, despite the inherent difficulty in preventing significant interaction between meteoric and pore waters in deep circulation, current data show no evidence of such interaction, implying that long-distance meteoric water migration did not occur; (iii) fluid activity associated with the compressional orogenic period's distal faults is a more compelling explanation.

During the first episode of the Middle Caledonian, compression from the closure of the West Kunlun Ocean on the basin's southwest margin resulted in brief surface exposure in parts of SHB (lasting under 1–2 Ma) (Chen et al., 2016). Evidence includes solution and casting pores, geopetal structures as per Wang et al. (2023), and karst breccia (Fig. 3(b)) atop the O₂yj in the No. 1 fault zone, indicating subdued historical hydrodynamic runoff. Thus, meteoric water intrusion's connection with the fault system is plausible (Fig. 11(a)). Recent studies indicate significant NEtrending regional joints in SHB, created by tectonic stress (Deng et al., 2021), which played a critical role in facilitating the downward movement of highly mineralized meteoric water, leading to the formation of C2 and C3. The closure of the Altyn ocean basin initiated strong compressive stress from the southeast (third episode of the Middle Caledonian movement), transforming

regional joints into strike-slip faults during the Upper Ordovician's thick clastic rock deposition (Fig. 11(c)). These evolving pathways facilitated surface meteoric water migration and sustained waterrock interactions, leading to ⁸⁷Sr-enriched VC cement formation in the Middle-Lower Ordovician, followed by clay mineral leaching. Simultaneously, subduction of the Middle Tianshan block towards the South Tianshan Ocean caused some uplift in SHB, while SN remained structurally lower (Huang, 2014). Consequently, meteoric water distribution was confined within SHB (Fig. 11(b)).

Considering these factors, SHB illustrates meteoric water intrusion in non-denudative areas, marked by crushed primary fractures and minimal fluid-induced fracture alteration. This model diverges from conventional buried hill weathering crust paleokarst (Raeisi and Mylroie, 1995; Lønøy et al., 2021), providing valuable insight into paleo-fluid activity. The precise tracing and semi-quantitative fluid flow range recovery in this study enhance future pore development zone prediction, supporting 'fault-controlled' and 'fault-solution-controlled' reservoir research concepts as a starting point for analogous basins.

6. Conclusion

Through the synthesis and amalgamation of petrological characteristics, this study identified six different types of matrix carbonate rocks and five variations of calcite cements. The matrix rocks primarily comprise grainstone (GS), wackstone (WS)/packstone (PS), and micritic limestone (ML), which exhibit typical seawater-calcite isotope values and remarkably low Mn/Sr ratios. The diverse calcite cements reflect variation in diagenetic fluids: the RFC and C1 minerals are derived from seawater, yet their relatively elevated Fe and Mn contents, peculiar Ce anomalies, flatter REY partitioning pattern, and higher SREE concentrations suggest that the precipitation of C1 may have occurred during the

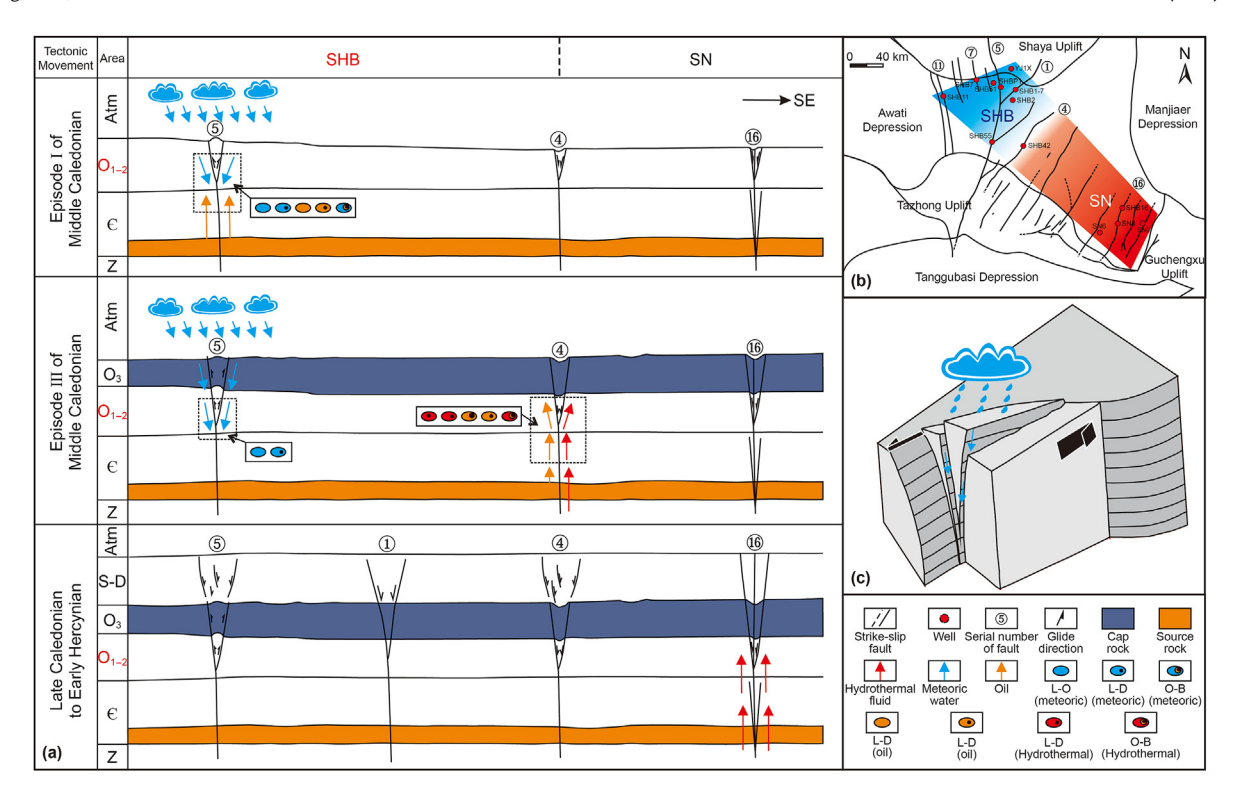


Fig. 11. (a) Schematic diagram of fluid flow mechanism; (b) Estimated range of meteoric water and hydrothermal fluid in the SLU; (c) Meteoric water intrusion pattern in the SHB.

eogenetic stage due to the activation of connate seawater preserved in the host limestone during a specific tectonic event, C2, C3, and VC with low ΣREE concentrations, low Y/Ho ratio, slightly convex and flat REY_{SN} profiles, and a melting temperature close to 0 °C in fluid inclusions provide compelling evidence for precipitation in meteoric water. Unlike the fluid source, the origin of the VC can be traced back to meteoric water extracted from the overlying strata. Consequently, these meteoric intrusion events are closely associated with the first and third episodes of the Middle Caledonian movement and are intricately linked to fault activity occurring at considerable distances from the orogenic belt and paleo-karst system. This study further enhances our previous findings by reaffirming the influence range of hydrothermal fluids and establishing a groundbreaking model for the evolution of diagenetic fluids. This is pivotal for advancing the scientific understanding of the intricate coupling effect between the structure and fluid in the SHB and guiding reservoir prediction throughout the entire basin.

CRediT authorship contribution statement

Bai-Wen Huang: Writing — original draft, Validation, Methodology, Formal analysis, Conceptualization. **Ning Ye:** Supervision. **Zi-Ye Lu:** Visualization, Data curation. **Bei Zhu:** Visualization, Resources. **Yi-Ming Yang:** Software. **Pan Lin:** Investigation. **Pei-Jie Li:** Software. **Xin-Yan Zhang:** Validation. **Ying-Tao Li:** Project administration. **Shao-Nan Zhang:** Supervision.

Declaration of competing interest

The authors declare that they have no known competing financial interests or personal relationships that could have appeared to influence the work reported in this paper.

Acknowledgements

This study was supported by the National Natural Science Foundation of China (42102191).

References

Arthur, H.S., 1986. Radiaxial calcite in lower Miocene strata, subsurface Enewetak Atoll. J. Sediment. Res. 56 (6), 743–762. https://doi.org/10.1306/212F8A3A-2B24-11D7-8648000102C1865D.

Balsamo, F., Storti, F., Gröcke, D.R., 2012. Fault-related fluid flow history in shallow marine sediments from carbonate concretions, Crotone basin, south Italy. J. Geol. Soc. 169, 613–626. https://doi.org/10.1144/0016-76492011-109.

Banner, J.L., 1995. Application of the trace element and isotope geochemistry of strontium to studies of carbonate diagenesis. Sedimentology 42 (5), 805–824. https://doi.org/10.1111/j.1365-3091.1995.tb00410.x.

Bartley, J.K., Semikhatov, M.A., Kaufman, A.J., Knoll, A.H., Jacobsen, S.B., 2001. Global events across the Mesoproterozoic-Neoproterozoic boundary: C and Sr isotopic evidence from Siberia. Precambr. Res. 111 (1), 165–202. https://doi.org/10.1016/ S0301-9268/01)00160-7.

Bau, M., Alexander, B.W., 2009. Distribution of high field strength elements (Y, Zr, REE, Hf, Ta, Th, U) in adjacent magnetite and chert bands and in reference standards FeR-3 and FeR-4 from the temagami iron-formation, Canada, and the redox level of the neoarchean ocean. Precambr. Res. 174, 337–346. https://doi.org/10.1016/i.precamres.2009.08.007.

Bau, M., Balan, S., Schmidt, K., Koschinsky, A., 2010. Rare earth elements in mussel shells of the Mytilidae family as tracers for hidden and fossil high-temperature hydrothermal systems. Earth Planetary Ence Lett. 299 (3–4), 310–316. https://doi.org/10.1016/j.epsl.2010.09.011.

Bau, M., Dulski, P., 1996. Distribution of yttrium and rare earth elements in the Penge and Kuruman iron-formations, Transvaal Supergroup, South Africa. Precambrain Res. 79, 37–55. https://doi.org/10.1016/0301-9268(95)00087-9.

Bayon, G., Birot, D., Ruffine, L., Caprais, J.C., Ponzevera, E., Bollinger, C., Donval, J.P., Charlou, J.L., Voisset, M., Grimaud, S., 2011. Evidence for intense REE scavenging at cold seeps from the Niger Delta margin. Earth Planet Sci. Lett. 312 (3–4), 443–452. https://doi.org/10.1016/j.epsl.2011.10.008.

Bolhar, R., Van Kranendonk, M.J., 2007. A non-marine depositional setting for the northern Fortescue Group, Pilbara Craton, inferred from trace element geochemistry of stromatolitic carbonates. Precambr. Res. 155 (3–4), 229–250. https://doi.org/10.1016/j.precamres.2007.02.002.

Brand, U., Veizer, J., 1980. Chemical diagenesis of a multicomponent carbonate system-1. Trace elements. J. Sediment. Res. 50 (4), 1219—1236. https://doi.org/10.1306/212F7BB7-2B24-11D7-8648000102C1865D.

Cao, Z.C., Lu, Q.H., Gu, Y., Wu, X., You, D.H., Zhu, X.X., 2020. Characteristics of Ordovician reservoirs in Shunbei 1 and 5 fault zones. Tarim Basin. Oil and Gas Geology 41 (5), 975–984. https://doi.org/10.11743/ogg20200508 (in Chinese).

- Cathles, L.M., Smith, A.T., 1983. Thermal constraints on the formation of Mississippi Valley-type lead—zinc deposits and their implications for episodic basin dewatering and deposit genesis. Econ. Geol. 78, 983—1002. https://doi.org/10.2113/gsecongen.78.5.983
- Chen, H.H., Wu, Y., Zhu, H.T., Lu, Z.Y., Cao, Z.C., Yun, L., 2016. Eogenetic karstification and reservoir formation model of the Middle-Lower Ordovician in the northeast slope of Tazhong uplift, Tarim Basin. Acta Pet. Sin. 37 (10), 1231–1246. https://doi.org/10.7623/syxb201610003 (in Chinese).
- Davies, G., Smith, L., 2006. Structurally controlled hydrothermal dolomite reservoir facies: an overview. AAPG (Am. Assoc. Pet. Geol.) Bull. 90 (11), 1641–1690. https://doi.org/10.1306/05220605164.
- De Carlo, E.H., Green, W.J., 2002. Rare earth elements in the water column of lake vanda, McMurdo dry valleys, Antarctica. Geochem. Cosmochim. Acta. 66 (8), 1323–1333. https://doi.org/10.1016/S0016-7037(01)00861-4.
- Deng, S., Li, H.L., Zhang, Z.P., Wu, X., Zhang, J.B., 2018. Characteristics of differential activities in major strike-slip fault zones and their control on hydrocarbon enrichment in Shunbei area and its surroundings, Tarim Basin. Oil Gas Geol. 39 (5), 878–888. https://doi.org/10.11743/ogg20180503 (in Chinese).
- Deng, S., Liu, Y.Q., Liu, J., Han, J., Wang, B., Zhao, R., 2021. Structural styles and evolution models of intracratonic strike-slip faults and the implications for reservoir exploration and appraisal: a case study of the Shunbei area, Tarim Basin. Geotect. Metallogenia 45 (6), 1111–1126. https://doi.org/10.16539/ j.ddgzyckx.2020.05.015 (in Chinese).
- Dong, S., Chen, D., Qing, H., Zhou, X., Wang, D., Guo, Z., Jiang, M., Qian, Y., 2013. Hydrothermal alteration of dolostones in the Lower Ordovician, Tarim Basin, NW China: multiple constraints from petrology, isotope geochemistry and fluid inclusion microthermometry. Mar. Petrol. Geol. 46, 270–286. https://doi.org/ 10.1016/j.marpetgeo.2013.06.013.
- Dworczak, P.G., Correa, M.L., Jakubowicz, M., Munnecke, A., Joachimski, M.M., Mazzoli, C., Berkowski, B., 2022. Carbon and oxygen isotope fractionation in the Late Devonian heterocoral Oligophylloides: implications for the skeletogenesis and evolution of the Heterocorallia. Palaeogeogr. Palaeoclimatol. Palaeoecol. 598. https://doi.org/10.1016/j.palaeo.2022.111017.
- Ehrenberg, S., Bjørlykke, K., 2016. Comments regarding hydrothermal dolomitization and porosity development in the paper "Formation mechanism of deep Cambrian dolomite reservoirs in the Tarim basin, northwestern China" by Zhu et al. (2015). Mar. Petrol. Geol. 76, 480–481. https://doi.org/10.1016/j.marpetgeo.2015.09.008.
- Elderfield, H., Sholkovitz, E.R., 1987. Rare earth elements in the pore waters of reducing nearshore sediments. Earth Planet Sci. Lett. 82, 280–288. https:// doi.org/10.1016/0012-821X(87)90202-0.
- Elisha, B., Nuriel, P., Kylander-Clark, A., Weinberger, R., 2021. Towards in situ U-Pb dating of dolomite. Geochronology 3, 337–349. https://doi.org/10.5194/GCHRON-3-337-2021.
- Franchi, F., Hofmann, A., Cavalazzi, B., Wilson, A., Barbieri, R., 2015. Differentiating marine vs hydrothermal processes in Devonian carbonatemounds using rare earth elements (Kess Kess mounds, Anti-Atlas, Morocco). Chem. Geol. 409, 69–86. https://doi.org/10.1016/j.chemgeo.2015.05.006.
- Frimmel, H.E., 2009. Trace element distribution in Neoproterozoic carbonates as palaeoenvironmental indicator. Chem. Geol. 258 (3–4), 338–353. https://doi.org/10.1016/j.chemgeo.2008.10.033.
- Goldstein, R.H., 2001. Fluid inclusions in sedimentary and diagenetic systems. Lithos 55, 159–193. https://doi.org/10.1016/s0024-4937(00)00044-x.
- Haley, B.A., Klinkhammer, G.P., McManus, J., 2004. Rare earth elements in pore waters of marine sediments. Geochem. Cosmochim. Acta. 68 (6), 1265–1279. https://doi.org/10.1016/j.gca.2003.09.012.
- Han, J., Kuang, A.P., Neng, Y., Huang, C., Li, Q.Q., Chen, P., Shen, Z.Y., 2021. Vertical layered structure of Shunbei No.5 strike-slip fault zone and its significance on hydrocarbon accumulation. Xinjing Pet. Geol. 42 (2), 152–160. https://doi.org/10.7657/XJPG20210204 (in Chinese).
- Han, X.Y., Tang, L.J., Cao, Z.C., Ying, S.Y., Wang, Y., Dong, G.Y., 2023. Characterization of intraplate strike-slip faults with small displacement: a case study of the Shunnan area, Tarim Basin. Geol. Rev. 69 (S1), 79–80. https://doi.org/10.16509/j.georeview.2023.s1.030 (in Chinese).
- Hannigan, R.E., Sholkovitz, E.R., 2001. The development of middle rare earth element enrichments in freshwaters: weathering of phosphate minerals. Chem. Geol. 175 (3–4), 495–508. https://doi.org/10.1016/S0009-2541(00)00355-7.
- Herwartz, D., Tütken, T., Jochum, K.P., Sander, P.M., 2013. Rare earth element systematics of fossil bone revealed by LA-ICP-MS analysis. Geochem. Cosmochim. Acta 103, 161–183. https://doi.org/10.1016/j.gca.2012.10.038.
- Hodson, K.R., Crider, J.G., Huntington, K.W., 2016. Temperature and composition of carbonate cements record early structural control on cementation in a nascent deformation band fault zone: moab Fault, Utah, USA. Tectonophysics 690 (A), 240–252. https://doi.org/10.1016/j.tecto.2016.04.032.
- Huang, B.W., Ye, N., Zhang, Y.M., Lu, Z.Y., Sui, H., Zhu, B., Zhang, S.N., Li, Y.T., 2022. Analysis of the origin of calcite cements and fluid sources in limestone formations based on petrology and geochemical data. Chem. Technol. Fuels Oils 58, 136–145. https://doi.org/10.1007/s10553-022-01361-z.
- Huang, T.Z., 2014. Structural interpretation and petroleum exploration targets in northern slope of middle Tarim Basin. Petroleum Geology and Experiment 36 (3), 257–267. https://doi.org/10.11781/sysydz201403257 (in Chinese).
- Jia, C.Z., Ma, D.B., Yuan, J.Y., Wei, G.Q., Yang, M., Yan, L., Tian, F.L., Jiang, L., 2021.

Structural characteristics, formation and evolution and genetic mechanisms of strike—slip faults in the Tarim Basin. Nat. Gas. Ind. 41 (8), 81—91. https://doi.org/10.3787/j.issn.1000-0976.2021.08.008 (in Chinese).

- Jiao, F.Z., 2017. Significance of oil and gas exploration in NE strike-slip fault belts in Shuntuoguole area of Tarim Basin. Oil Gas Geol. 38 (5), 831–839. https:// doi.org/10.11743/ogg20170501 (in Chinese).
- Kaufman, A.J., Hayes, J.M., Knoll, A.H., Germs, G.J.B., 1991. Isotopic compositions of carbonates and organic carbon from upper Proterozoic successions in Namibia: stratigraphic variation and the effects of diagenesis and metamorphism. Precambr. Res. 49 (3), 301–327. https://doi.org/10.1016/0301-9268(91)90039-D.
- Kaufman, A.J., Knoll, A.H., 1995. Neoproterozoic variations in the C-isotopic composition of seawater: stratigraphic and biogeochemical implications. Precambr. Res. 73 (1–4), 27–49. https://doi.org/10.1016/0301-9268(94)00070-8.
- Kendall, A.C., Tucker, M.E., 2010. Radiaxial fibrous calcite: a replacement after acicular carbonate. Sedimentology 20 (3), 365–389. https://doi.org/10.1111/ i.1365-3091.1973.tb01616.x.
- Kowal-Linka, M., Jochum, K.P., Surmik, D., 2014. LA- ICP-MS analysis of rare earth elements in marine reptile bones from the Middle Triassic bonebed (Upper Silesia, S Poland): impact of long-lasting diagenesis, and factors controlling the uptake. Chem. Geol. 363 (10), 213–228. https://doi.org/10.1016/ j.chemgeo.2013.10.038.
- Lambert, L., Durlet, C., Loreau, J.P., Marnier, G., 2006. Burial dissolution of micrite in Middle East carbonate reservoirs (Jurassic-Cretaceous): keys for recognition and timing. Mar. Petrol. Geol. 23 (1), 79–92. https://doi.org/10.1016/ j.marpetgeo.2005.04.003.
- Li, C.X., Wang, X.F., Li, B.L., He, D.F., 2013. Paleozoic fault systems of the tazhong uplift, Tarim Basin, China. Mar. Petrol. Geol. 39 (1), 48–58. https://doi.org/10.1016/j.marpetgeo.2012.09.010.
- Li, F., Webb, G.E., Algeo, T.J., Kershaw, S., Lu, C.J., Oehlert, A.M., Gong, Q.L., Pourmand, A., Tan, X.C., 2019. Modern carbonate ooids preserve ambient aqueous REE signatures. Chem. Geol. 509, 163–177. https://doi.org/10.1016/ j.chemgeo.2019.01.015.
- Li, H.L., Gao, J., Cao, Z.C., Zhu, X.X., Guo, X.W., Zeng, S., 2023. Spatial-temporal distribution of fluid activity and hydrocarbon accumulation significance in the strike-slip fault zones of Shuntuoguole low-uplift in Tarim Basin. Earth Sci. Front. 1–13. https://doi.org/10.13745/j.esf.sf.2023.2.36 (in Chinese).
- Li, Y.T., Ye, N., Yuan, X.Y., Huang, Q.Y., Su, B.R., Zhou, R.Q., 2015. Geological and geochemical characteristics of silicified hydrothermal fluids in Well Shunnan 4, Tarim Basin. Oil Gas Geol. 36 (6), 934–944. https://doi.org/10.11743/ogg20150608 (in Chinese).
- Longman, M.W., 1980. Carbonate diagenetic texture from nearsurface diagenetic environment. AAPG Bull. 64, 461–487. https://doi.org/10.1007/BF01081857.
- Lønøy, B., Pennos, C., Tveranger, J., Fikos, I., Vargemezis, G., Lauritzen, S.E., 2021. Delimiting morphological and volumetric elements of cave surveys as analogues for paleokarst reservoir modelling-A case study from the maaras cave system, northern Greece. Mar. Pet. Geology. 129, 105091. https://doi.org/10.1016/j.marpetgeo.2021.105091.
- Lottermoser, B.G., 1992. Rare earth elements and hydrothermal ore formation processes. Ore Geol. Rev. 7 (1), 25–41. https://doi.org/10.1016/0169-1368(92)
- Lu, Z.Y., Chen, H.H., Qing, H.R., Chi, G.X., You, D.H., Yin, H., Zhang, S.Y., 2017. Petrography, fluid inclusion and isotope studies in Ordovician carbonate reservoirs in the Shunnan area, Tarim basin, NW China: implications for the nature and timing of silicification. Sediment. Geol. 359 (15), 29–43. https://doi.org/10.1016/j.sedgeo.2017.08.002.
- Lu, Z.Y., Li, Y.T., Ye, N., Zhang, S.N., Lu, C.J., Li, W., Cheng, Z., Ding, X.Q., Zhu, B., Huang, B.W., 2020. Fluid inclusions record hydrocarbon charge history in the Shunbei area, Tarim Basin, NW China. Geofluids 2020. https://doi.org/10.1155/ 2020/18847247
- Lv, H.T., Han, Y., Zhang, J.B., Liu, Y.L., Li, Y.T., 2021. Development characteristics and formation mechanism of ultra-deep carbonate fault-dissolution body in Shunbei area, Tarim Basin. Petroleum Geology and Experiment 43 (1), 14–22. https://doi.org/10.11781/sysydz202101014 (in Chinese).
- Machel, H.G., 2004. Concepts and models of dolomitization: a critical reappraisal. Geological Society, London, Special Publications 235 (1), 7–63. https://doi.org/10.1144/GSL.SP.2004.235.01.02.
- Machel, H.G., Buschkuehle, B.E., Michael, K., 2002. Squeegee flow in Devonian carbonate aquifers in Alberta, Canada. In: Proceedings of the 2002 Annual Meeting of the Geological Association of Canada. Geological Association of Canada.
- Mazzullo, S.J., Bischoff, W.D., Lobitzer, H., 2010. Diagenesis of radiaxial fibrous calcites in a subunconformity, shallow-burial setting: upper Triassic and Liassic, Northern Calcareous Alps, Austria. Sedimentology 37 (3), 407–425. https://doi.org/10.1111/j.1365-3091.1990.tb00144.x.
- Meyer, E.E., Quicksall, A.N., Landis, J.D., Link, P.K., Bostick, B.C., 2012. Trace and rare earth elemental investigation of a Sturtian cap carbonate, Pocatello, Idaho: evidence for ocean redox conditions before and during carbonate deposition. Precambr. Res. 192—195, 89—106. https://doi.org/10.1016/j.precamres.2011.09.015.
- Nan, J.Y., Liu, Y.Y., 2004. Organic and inorganic carbon-isotope shift and paleo-environment at the P-T boundary section in Meishan, Zhejiang Province. Geochemica 33 (1), 9–19. https://doi.org/10.19700/j.0379-1726.2004.01.002 (in Chinese).
- Nasir, S., Al-Saad, H., Alsayigh, A., Weidlich, O., 2008. Geology and petrology of the hormuz dolomite, infra-cambrian: implications for the formation of the salt-

cored halul and shraouh islands, offshore, state of Qatar. J. Asian Earth Sci. 33 (5–6), 353–365. https://doi.org/10.1016/j.jseaes.2008.02.003.

- Navarro-Ciurana, D., Corbella, M., Cardellach, E., Vindel, E., Gómez-Gras, D., Griera, A., 2016. Petrography and geochemistry of fault-controlled hydrothermal dolomites in the Riópar area (Prebetic Zone, SE Spain). Mar. Petrol. Geol. 71, 310–328. https://doi.org/10.1016/j.marpetgeo.2016.01.005.
- Nothdurft, L.D., Webb, G.E., Kamber, B.S., 2004. Rare earth element geochemistry of Late Devonian reefal carbonates, Canning Basin, Western Australia: confirmation of a seawater REE proxy in ancient limestones. Geochem. Cosmochim. Acta. 68 (2), 263–283. https://doi.org/10.1016/S0016-7037(03)00422-8.
- Nozaki, Y., Lerche, D., Alibo, D.S., Snidvongs, A., 2000. The estuarine geochemistry of rare earth elements and indium in the Chao Phraya River, Thailand. Geochem. Cosmochim. Acta. 64 (23), 3983–3994. https://doi.org/10.1016/S0016-7037(00) 00473-7.
- Planavsky, N., Bekker, A., Rouxel, O.J., Kamber, B., Hofmann, A., Knudsen, A., Lyons, T.W., 2010. Rare earth element and yttrium compositions of Archean and Paleoproterozoic Fe formations revisited: new perspectives on the significance and mechanisms of deposition. Geochem. Cosmochim. Acta. 74 (22), 6387—6405. https://doi.org/10.1016/j.gca.2010.07.021.
- Qing, H., Mountjoy, E., 1992. Large-scale fluid-flow in the middle devonian presquile barrier, western Canada sedimentary basin. Geology 20 (10), 903–906. https://doi.org/10.1130/0091-7613(1992)0202.3.CO:2.
- Qiu, H.B., Deng, S., Cao, Z.C., Yin, T., Zhang, Z.P., 2019. The evolution of the complex anticlinal belt with crosscutting strike-slip faults in the central Tarim Basin, NW China. Tectonics 38 (6), 2087—2113. https://doi.org/10.1029/2018TC005229. Raeisi, E., Mylroie, J.E., 1995. Hydrodynamic behavior of caves formed in the fresh-
- Raeisi, E., Mylroie, J.E., 1995. Hydrodynamic behavior of caves formed in the freshwater lens of carbonate islands. Carbonates Evaporites 10 (2), 207–214. https://doi.org/10.1007/BF03175405.
- Rasbury, E.T., Present, T.M., Northrup, P., Tappero, R.V., Lanzirotti, A., Cole, J.M., Wooton, K.M., Hatton, K., 2021. Tools for uranium characterization in carbonate samples: case studies of natural U-Pb geochronology reference materials. Geochronology 3, 103–122. https://doi.org/10.5194/gchron-3-103-2021.
- Rikke, W., Henrik, F., Kazerouni, M.A., Svendsen, J.B., Stokkendal, J., Poulsen, M.L.K., 2010. Development of early diagenetic silica and quartz morphologies: example from the Siri Canyon, Danish North Sea. Sediment. Geol. 228 (3–4), 151–170. https://doi.org/10.1016/j.sedgeo.2010.04.008.
- Robbins, L.J., Lalonde, S.V., Planavsky, N.J., Partin, C.A., Reinhard, C.T., Kendall, B., Scott, C., Hardisty, D.S., Gill, B.C., Alessi, D.S., Dupont, C.L., Saito, M.A., Crowe, S.A., Poulton, S.W., Bekker, A., Lyons, T.W., Konhauser, K.O., 2016. Trace elements at the intersection of marine biological and geochemical evolution. Farth Sci. Rev. 163, 323–348. https://doi.org/10.1016/j.earscirev.2016.10.013
- Earth Sci. Rev. 163, 323—348. https://doi.org/10.1016/j.earscirev.2016.10.013. Roberts, N.M.W., Waker, R.J., 2016. U-Pb geochronology of calcite-mineralized faults: absolute timing of rift-related fault events on the Northeast Atlantic Margin. Geology 44 (7), 531—534. https://doi.org/10.1130/G37868.1.
- Shen, A.J., Hu, A.P., Cheng, T., Liang, F., Pan, W.Q., Feng, Y.X., Zhao, J.X., 2019. Laser ablation in situ U-Pb dating and its application to diagenesis-porosity evolution of carbonate reservoirs. Petrol. Explor. Dev. 46 (6), 1062–1074. https://doi.org/10.1016/s1876-3804(19)60268-5.
- Sibley, D.F., Gregg, J.M., 1987. Classification of dolomite rock textures. J. Sediment. Res. 57 (5), 967–975. https://doi.org/10.1306/212F8B9B-2B24-11D7-8648000102C1865D.
- Smye, A.J., Marsh, J.H., Vermeesch, P., Garber, J.M., Stockli, D.F., 2018. Applications and limitations of U-Pb thermochronology to middle and lower crustal thermal histories. Chem. Geol. 494, 1–18. https://doi.org/10.1016/ j.chemgeo.2018.07.003.
- Song, G., Li, H.Y., Ye, N., Han, J., Xiao, C.Y., Lu, Z.Y., Li, Y.T., 2022. Types and features of diagenetic fluids in Shunbei No. 4 strike-slip fault zone in Shuntuoguole low uplift, Tarim Basin. Petroleum Geology and Experiment 44 (4), 603–612. https://doi.org/10.11781/sysydz202204603 (in Chinese).
- Stacey, J., Corlett, H., Holland, G., Koeshidayatullah, A., Cao, C., Swart, P., Crowley, S., Hollis, C., 2021. Regional fault-controlled shallow dolomitization of the Middle Cambrian Cathedral Formation by hydrothermal fluids fluxed through a basal clastic aquifer. Geol. Soc. Am. Bull. 133 (11–12), 2355–2377. https://doi.org/ 10.1130/B35927.1.
- Su, A., Chen, H.H., Feng, Y.X., Zhao, J.X., Wang, Z.C., Hu, M.Y., Jiang, H., Nguye, A.D.,

- 2022. In situ U-Pb dating and geochemical characterization of multistage dolomite cementation in the Ediacaran Dengying Formation, Central Sichuan Basin, China: constraints on diagenetic, hydrothermal and paleo-oil filling events. Precambr. Res. 368, 106481. https://doi.org/10.1016/j.precamres.2021.106481.
- Sylvestre, G., Evine Laure, N.T., Gus Djibril, K.N., Arlette, D.S., Cyriel, M., Timoléon, N., Jean Paul, N., 2017. A mixed seawater and hydrothermal origin of superior-type banded iron formation (BIF)-hosted Kouambo iron deposit, Palaeoproterozoic Nyong series, Southwestern Cameroon: constraints from petrography and geochemistry. Ore Geol. Rev. 80, 860–875. https://doi.org/10.1016/i.orggeorev.2016.08.021.
- Tachikawa, K., Jeandel, C., Vangriesheim, A., Dupré, B., 1999. Distribution of rare earth elements and neodymium isotopes in suspended particles of the tropical Atlantic Ocean (EUMELI site). Deep-Sea Res. I Oceanogr. Res. Pap. 46, 733–755. https://doi.org/10.1016/s0967-0637(98)00089-2.
- Tong, X.R., Liu, Y.S., Hu, Z.C., Chen, H.H., Zhou, L., Hu, Q.H., Xu, R., Deng, L.X., Chen, C.F., Yang, L., Gao, S., 2016. Accurate determination of Sr isotopic compositions in clinopyroxene and silicate glasses by LA-MC-ICP-MS. Geostand. Geoanal. Res. 40 (1), 85–99. https://doi.org/10.1111/j.1751-908X.2015.00315.x.
- Tostevin, R., Shields, G.A., Tarbuck, G.M., He, T., Clarkson, M.O., Wood, R.A., 2016. Effective use of cerium anomalies as a redox proxy in carbonate-dominated marine settings. Chem. Geol. 438, 146–162. https://doi.org/10.1016/j.chemgeo.2016.06.027.
- Tribovillard, N., Algeo, T.J., Lyons, T., Riboulleau, A., 2006. Trace metals as paleoredox and paleoproductivity proxies: an update. Chem. Geol. 232 (1–2), 12–32. https://doi.org/10.1016/j.chemgeo.2006.02.012.

 Tucker, M.E., Wright, V.P., 1990. Carbonate Sedimentology. Wiley-Blackwell, Oxford.
- Tucker, M.E., Wright, V.P., 1990. Carbonate Sedimentology. Wiley-Blackwell, Oxford.
 Veizer, J., Ala, D., Azmy, K., Bruckschen, P., Buhl, D., Bruhn, F., Carden, G.A.F., Diener, A., Ebneth, S., Godderis, Y., Jasper, T., Korte, C., Pawellek, F., Podlaha, O.G., Sreauss, H., 1999. ⁸⁷Sr/8⁶Sr, δ¹³C and δ¹⁸O evolution of Phanerozoic seawater. Chem. Geol. 161 (1–3), 59–88. https://doi.org/10.1016/S0009-2541(99)00081-
- Wang, B., 2022. Diagenetic Fluid Evolution and Dynamic Accumulation Process of Strike Slip Fault Zone in the North of Shuntoguole Low Uplift. China University of Geosciences. https://doi.org/10.27492/d.cnki.gzdzu.2022.000155 (in Chinese).
- Wang, Y.W., Chen, H.H., Cao, Z.C., Yun, L., 2023. Controlling effects of fluid activity on reservoir formation in Shunbei area. Fault-Block Oil Gas Field 30 (1), 44–51. https://doi.org/10.6056/dkyqt202301007 (in Chinese).
- Warren, J., 2000. Dolomite: occurrence, evolution and economically important associations. Earth Sci. Rev. 52 (1–3), 1–81. https://doi.org/10.1016/S0012-8252(00)00022-2.
- Webb, G.E., Kamber, B.S., 2000. Rare earth elements in Holocene reefal microbialites: a new shallow seawater proxy. Geochim Cosmochim Acta 64 (9), 1557–1565. https://doi.org/10.1016/S0016-7037(99)00400-7.
- Woo, K.S., Anders, T.F., 1993. Diagenesis of skeletal and nonskeletal components of mid-Cretaceous limestones. J. Sediment. Res. 63 (1), 18–32. https://doi.org/ 10.1306/D4267A7D-2B26-11D7-8648000102C1865D.
- Worden, R.H., French, M.W., Marinal, E., 2012. Amorphous silica nanofilms result in growth of misoriented microcrystalline quartz cement maintaining porosity in deeply buried sandstones. Geology 40 (2), 179–182. https://doi.org/10.1130/g32661.1.
- Yapparova, A., Yapparova, A., Gabellone, T., Whitaker, F., Kulik, D.A., Matthäi, S.K., 2017. Reactive transport modelling of hydrothermal dolomitisation using the CSMP++GEM coupled code: effects of temperature and geological heterogeneity. Chem. Geol. 466, 562–574. https://doi.org/10.1016/j.chemgeo.2017.07.005.
- Ye, N., Li, Y.T., Huang, B.W., Xi, B.B., Jiang, H., Lu, Z.Y., Chen, Q.L., You, D.H., Xu, J., 2022. Hydrothermal silicification and its impact on lower—middle ordovician carbonates in shunnan area, Tarim Basin, NW China. Geol. J. 57 (9), 3538—3557. https://doi.org/10.1002/gj.4482.
- Zhao, Y.Y., Li, S.Z., Li, D., Guo, L.L., Dai, L., Tao, J.L., 2019. Rare earth element geochemistry of carbonate and its paleoenvironmental implications. Geotect. Metallogenia 43 (1), 141–167. https://doi.org/10.16539/j.ddgzyckx.2019.01.011 (in Chinese).